A quantitative in vivo CRISPR-imaging platform identifies regulators of hyperplastic and hypertrophic adipose morphology in zebrafish

Rebecca Wafer*, Panna Tandon* and James E. N. Minchin#

Institute for Neuroscience and Cardiovascular Research, Edinburgh BioQuarter, College of Medicine and Veterinary Medicine, University of Edinburgh, Scotland, United Kingdom, EH16 4SB

* Indicates equal contributions. # indicates author for correspondence: james.minchin@ed.ac.uk

Abstract

Adipose tissues exhibit a remarkable capacity to expand, regress, and remodel in response to energy status. The cellular mechanisms underlying adipose remodelling are central to metabolic health. Hypertrophic remodelling - characterised by the enlargement of existing adipocytes - is associated with insulin resistance, type 2 diabetes, and cardiovascular disease. In contrast, hyperplastic remodelling – in which new adipocytes are generated - is linked to improved metabolic outcomes. Despite its clinical importance, the regulation of hypertrophic and hyperplastic adipose morphology remains poorly understood. Here, we integrate human transcriptomic data with a quantitative CRISPR-imaging platform in zebrafish to identify regulators of adipose morphology. We developed an image-based phenotyping pipeline that captures lipid droplet size, number, and spatial patterning, and applied generalised additive modelling to quantify hyperplastic versus hypertrophic morphology signatures. Using this platform, we conducted an F0 CRISPR screen targeting 25 candidate genes and identified three that induced hypertrophic morphology (*txnipa*, *mmp14b* and *foxp1b*) and an additional candidate that altered total adiposity (*kazna*). For functional validation, we generated stable loss-of-function alleles for both zebrafish foxp1 paralogues. Spatial analysis along the anterior-posterior axis revealed that *foxp1b* mutants display developmental hypertrophy but profoundly blunted adaptive responses to high-fat diet (~68% reduction across all spatial zones), while *foxp1a* mutants show normal baseline morphology but disrupted spatial patterning of diet-induced hypertrophy. Together, these findings establish a scalable CRISPR-imaging platform for in vivo genetic screening of adipose morphology, and reveal distinct roles for Foxp1 paralogues in developmental patterning and adaptive responses to dietary challenge in adipose tissue.

Introduction

Adipose tissues exhibit a remarkable capacity to remodel and restructure themselves in response to the energetic status, the environment, physiological demands, or disease. Adipose remodelling involves alterations in both adipocyte number (addition or removal of adipocytes) and adipocyte size (expansion or reduction in adipocyte size). Increases in adipocyte size (hypertrophy) can trigger hypoxia, necrosis, altered lipid flux, inflammation and insulin resistance (1–3). Accordingly, a hypertrophic adipose morphology – adipose characterised by few, large adipocytes – is associated with increased cardiometabolic disease (4–6). Contrastingly, a hyperplastic adipose morphology - characterised by many, small adipocytes - is associated with more metabolically beneficial outcomes (7,8). Indeed, reductions in the hyperplastic potential of mouse adipose is associated with decreased insulin sensitivity (9), and disruption of adipocyte progenitor differentiation, proliferation and renewal leads to adipose hypertrophy and ensuing metabolic dysfunction (10). Strikingly, adipose hypertrophy is increased and preadipocyte frequency is reduced in diabetic obese patients (relative to non-diabetic obese) (11), and genetic predisposition for Type 2 diabetes, but not obesity, is

50 associated with an impaired ability to recruit new adipose cells to store excess lipids in the
51 subcutaneous adipose tissue (12). Despite its clinical relevance, the genetic and cellular processes
52 that determine hyperplastic versus hypertrophic adipose morphology remain poorly understood, and
53 whether early developmental patterning of adipose morphology influences subsequent capacity for
54 adaptive remodelling remains an open question.

55

56 The zebrafish provides a tractable and powerful in vivo model for studying adipose growth and
57 remodelling dynamics. Zebrafish adipose tissue is morphologically similar to mammalian white
58 adipose tissue, comprising large adipocytes with a single dominant cytoplasmic lipid droplet (13,14).
59 Transcriptomic profiling further supports this conservation, with RNA-Seq data revealing strong
60 molecular similarity between zebrafish and mammalian white adipose tissue (15). Functionally,
61 zebrafish adipose depots respond dynamically to nutritional status - expanding following a high-fat
62 diet and regressing following food restriction (16,17). Further, prolonged high-fat or overfeeding has
63 been shown to induce diabetic phenotypes in zebrafish (18,19), reinforcing the model's relevance to
64 metabolic disease. One of the key advantages of the zebrafish model is its optical accessibility and
65 amenability to fluorescent imaging. Lipophilic dyes such as Nile Red can be used to label lipid droplets
66 (LDs) in vivo (13,20), and LD-associated protein reporters now allow real-time visualisation of lipid
67 droplet dynamics in living animals enabling rapid assessment of adiposity and LD morphology (21,22).
68 Additionally, transgenic tools are increasingly available to label and manipulate zebrafish adipocytes
69 (23,24). Importantly, zebrafish are amenable to high-throughput CRISPR mutagenesis, and recent
70 studies have combined F0 screens with quantitative imaging to examine candidate obesity genes
71 (25,26). However, existing approaches have focussed on total adiposity rather than cellular
72 composition of adipose tissue. To date, no scalable platform exists to quantify hyperplastic versus
73 hypertrophic adipose morphology in vivo – a gap that limits systematic genetic dissection of adipose
74 growth properties.

75

76 Here, we integrate human transcriptomic data with a quantitative CRISPR-imaging platform in
77 zebrafish to identify regulators of adipose morphology. We developed an image-based phenotyping
78 pipeline that captures lipid droplet size, number, and spatial patterning within subcutaneous adipose,
79 and applied generalised additive modelling to quantify hyperplastic versus hypertrophic morphology

80 signatures. Using this platform, we screened 25 candidate genes and identified three that induced
81 hypertrophic morphology (*txnipa*, *mmp14b* and *foxp1b*) and one that increased total adiposity
82 (*kazna*). For functional validation, we focused on Foxp1, a transcription factor known to regulate
83 stem and progenitor cell maintenance across multiple tissues. We generated stable loss-of-function
84 alleles for both zebrafish *foxp1* paralogues and performed spatial analysis of lipid droplet dynamics
85 along the anterior-posterior axis. This revealed that *foxp1b* mutants display developmental
86 hypertrophy but show profoundly blunted adaptive responses to high-fat diet, while *foxp1a* mutants
87 show normal baseline morphology but altered spatial patterning of diet-induced hypertrophy. These
88 findings suggest distinct roles for Foxp1 paralogues in developmental patterning versus adaptive
89 remodelling of adipose tissue.

90

91 # Methods

92 ## Identification of differentially expressed genes associated with small or large adipocytes in
93 human subcutaneous adipose

94 Differentially expressed genes (DEGs) associated with large or small adipocytes in human SAT were
95 obtained from Honecker et al., 2022. Briefly, 3,727 genes were significantly associated with adipocyte
96 area by both categorical and continuous statistical models (FDR < 0.05) (27). 2,190 DEGs were
97 associated with small adipocyte area, 1,537 DEGs associated with large adipocyte area (**Suppl. Table**
98 **1**). Expression within human WAT cell types for each of the candidate morphology genes was
99 determined using data from (28) via the Single Cell Portal
100 (https://singlecell.broadinstitute.org/single_cell). Scaled mean expression for each of the
101 morphology DEGs was assessed within each of the 16 previously defined WAT cell clusters (adipose
102 stem and progenitor cells (ASPCs), mesothelium, pericyte, adipocyte, macrophage, endothelial, LEC,
103 monocyte, T cells, dendritic cells, smooth muscle cells, b cells, mast cells, natural killer cells,
104 endometrium, and neutrophils). Of the 3,727 morphology genes, the following were removed: 410
105 genes without annotations in bulk RNA-Seq dataset, 250 genes not found in the Single Cell Portal
106 dataset, and 87 genes not expressed in the 16 WAT cell types. Hierarchical clustering of the remaining
107 2,980 morphology genes based on WAT cell type expression was performed in Morpheus
108 (https://software.broadinstitute.org/morpheus) using an average linkage method and one minus
109 Pearson correlation metric (**Suppl. Fig. 1**). Morphology genes enriched in ASPCs were identified as

110 either (i) belonging to the 75 morphology DEGs within the ASPC cluster, or (ii) one of the top 50
111 morphology DEGs with highest scaled mean expression in ASPCs (**Suppl. Table 2**). Three genes were
112 present in both categories (*CXCL14*, *KAZN* and *SPARC*), resulting in 122 ASPC-enriched morphology
113 DEGs (**Suppl. Table 2**). Ribosomal genes were excluded along with genes that did not code for
114 proteins, resulting in 102 candidate morphology genes (**Suppl. Table 2**).

115

116 Prioritisation and ranking of candidate adipose morphology genes

117 Enrichment analysis on the 102 candidate genes described above was performed using GProfiler
118 (https://biit.cs.ut.ee/gprofiler/gost), with the 3,727 original genes as a background gene set. Six
119 enriched GO biological process gene sets were identified, comprising; three 'developmental' terms
120 (GO:0048869, GO:0009888 & GO:0032502), one 'differentiation' term (GO:0030154), and two more
121 generic 'process' terms (GO:0048869 & GO:0048523) (**Suppl. Table 3**). For each of the 102
122 morphology genes, beta coefficients between SAT expression levels and the 23 cardiometabolic traits
123 from the METSIM study were clustered in Heatmapper (www.heatmapper.ca) using an average
124 linkage clustering method and Pearson distance measurement method (**Suppl. Fig. 2**). Correlations
125 between SAT expression and 23 cardiometabolic traits from 770 males as part of the METSIM study
126 were obtained from (29). The following genes were not found in the METSIM data: *EIF4EBP3*, *PDF*,
127 *SELENOM* and *SELENOS*. Candidate body mass index (BMI) and waist-to-hip ratio (WHR) genome-
128 wide association study (GWAS) genes were identified by (i) downloading summary statistics for BMI
129 and WHR from the GWAS Catalog (https://www.ebi.ac.uk/gwas/), (ii) identifying unique variants
130 associated with the traits at genome-wide significance ($p < 5 \times 10^{-8}$), (iii) calculating proxy variants in
131 in high linkage disequilibrium in CEU population ($R2>0.8$), (iv) calculating 'LD blocks' that encompass
132 each lead and associated proxy variants and (v) identifying genes that overlap with the LD blocks. The
133 DIOPT Ortholog Finder (https://www.flyrnai.org/cgi-bin/DRSC_orthologs.pl) was used to identify
134 zebrafish orthologs of the candidate human morphology genes based on the weighted score. The
135 'alignment & scores' function in DIOPT was used to calculate protein similarity between human and
136 zebrafish genes. scRNA-Seq scaled mean expression and % of cells expressing candidate genes from
137 Yang Loureiro et al. (2023) were obtained from the Single Cell Portal.

138

139 Zebrafish husbandry and maintenance

140 Zebrafish were housed in the Queen's Medical Research Institute (QMRI) facility at the University of
141 Edinburgh, UK. Standard husbandry was followed on a recirculating system and a 14h:10h light to
142 dark cycle. Feeding regimen was as described in Tandon et al., 2025. The wild-type line used were
143 WIKs maintained at the QMRI facility. Zebrafish experiments were conducted in accordance with the
144 UK Animals (Scientific Procedures) Act 1986 under the project licence PP9112175.

145

146 F0 CRISPR screen in zebrafish

147 We followed general CRISPR screen methodology (30–32). Between three and five guide RNAs
148 (gRNAs) were designed to target each gene using the UCSC Genome browser track
149 ZebrafishGenomics (31) and CHOPCHOP software. gRNAs were selected based on off-target and
150 efficiency scores, along with location in gene (targeting early exons, functional domains, and avoiding
151 exons with lengths divisible by three). Pooled in vitro transcription of gRNAs was performed as per
152 Wu et al (2018), and RNA was cleaned using Zymoclean columns (Zymo Research, Cat. # R1013). Prior
153 to injection, gRNAs were incubated with Cas9 protein (New England Biolabs, Cat. # M0646T) and
154 heated for 5 mins at 37°C. Mutagenesis of individual gRNAs was verified using T7E1 assays (New
155 England Biolabs, Cat. # M0302S). gRNAs were injected into zebrafish embryos at the one-cell stage
156 as per Wu et al 2018, along with a Fast Green dye to screen for successfully injected embryos.
157 Identical injection mixes lacking the gRNAs (Cas9-only control) were used for control groups. 50
158 injected embryos were placed per petri dish and screened for survival at 5 days post fertilisation
159 (dpf). At 5 dpf, injected larvae were placed in a small volume of system water in a 1L nursery tank
160 without running water. From 10 dpf, a slow flow of system water was introduced. Larvae were raised
161 at a density of 25 per 1L nursery tank, before being transferred to a 3L tank at 21 dpf. Survival was
162 further assessed at 21 dpf. Feeding regimen was as described for standard husbandry. At 36-42 dpf,
163 fish were euthanised and Nile Red staining performed as described previously (16).

164

165 Generation of *foxp1a* and *foxp1b* mutant zebrafish lines

166 *foxp1a* and *foxp1b* zebrafish mutant lines were made using standard CRISPR-Cas9 methods (34). For
167 both genes we targeted the highly conserved DNA-binding Forkhead domain (FHD). The location and
168 sequence of the CRISPR gRNAs were: *foxp1a* – 5'-GACGAGTGGAGAATGTGAAG-3' targeting the FHD

169 in exon 14, and *foxp1b* – 5'-GATAACGAAGCATACGTGAA-3' targeting the FHD in exon 15. We
170 generated two alleles - ed116 is a 13bp indel in the forkhead domain of *foxp1a* resulting in a
171 frameshift and premature stop codon, and ed125 is a 4bp indel in the forkhead domain of *foxp1b*
172 resulting in a frameshift and premature stop. Primers to amplify locus surrounding lesions for T7E1
173 assays or sequencing were: ed116 forward – 5'-GCCAGATTGGACTGGATGTT-3', ed116 reverse – 5'-
174 TTATTTCCAGGCCATTCTGG-3', ed125 forward – 5'-TTCAGTTTCAGCTCCTTCCTTC-3', ed125 reverse –
175 5'-TGGAAGTCAAGCTACCAGCA-3'. To genotype ed116, primers were designed to recognise wither
176 the 13bp indel or the wild-type sequence. Sequences were: forward – 5'-GCCAGATTGGACTGGATGTT-
177 3', reverse - 5'-TTATTTCCAGGCCATTCTGG-3', wild-type – 5'-ACGAGTGGAGAATGTGAAGG-3', ed116
178 – 5'-AAACGGCCCCCTCGTACT-3'. For ed125, the following primers were used to amplify the locus:
179 forward – 5'-TTCAGTTTCAGCTCCTTCCTTC-3', and reverse – 5'-TGGAAGTCAAGCTACCAGCA-3'. The
180 PCR product was then digested with the restriction enzyme HpyCH4IV (New England Biolabs, Cat. #
181 R0619S). Additionally, KASP genotyping assays were designed for the ed116 and ed125 alleles (KASP
182 on demand, LGC Biosearch Technologies). Western blots were performed to assess effect of
183 mutations on Foxp1 protein. Protein was isolated from the caudal fin - a pool of seven fin samples
184 was placed on dry ice in RIPA buffer (Thermo, Cat. # 8990) containing protease inhibitor (Thermo,
185 Cat. # A32953). Samples were homogenised with a TissueRupter, centrifuged for 15 mins at 4C, lysate
186 removed and added to LDS blue (Novex, Cat. # B0008) with reducing agent (Novex, B0009), heated
187 to 95C for 10 mins and the centrifuged for 1 min. Protein samples were run on 8% Bis-Tris gels
188 (Invitrogen, NW00082BOX) and run together with protein ladder (Thermo Scientific, Cat. # 26619).
189 Foxp1 antibody was PA5-26848 (Thermo Fisher) and b-actin antibody was (Sigma, A2228). Blood
190 assays were from Biovision (Glucose – K606-100, triacylglyceride – K622-100, cholesterol – K623-100)
191 and performed as per the manufacturer's instructions with 1 ul of blood from an adult zebrafish used
192 for the glucose and cholesterol assays, and 0.2 ul for the triacyclglyceride assay. qRT-PCR was
193 performed on a Roche LightCycler 480 using Luna reagents (New England Biolabs, Cat. # M3003L).
194 cDNA was synthesised using Superscript IV (Invitrogen, Cat. # 18090010). Primers were: *foxp1a*
195 forward 5'-GGCCACTTTGAGGATGACTC-3', *foxp1a* reverse 5'-CCTCGCCACCTAAAACTCAG-3', *foxp1b*
196 forward 5'-CATTGGCTCCTCTTTTACGC-3', *foxp1b* reverse 5'-ACAGCAACGGTAGTGACAGC-3', *bactin*
197 forward 5'-GCCTCCGATCCAGACAGAGT-3' and *bactin* reverse 5'-TGACAGGATGCAGAAGGAGA-3'.

198

199 **High-fat diet in zebrafish**

200 A high-fat immersion diet was conducted on juvenile fish at 35 dpf. Genotyped fish were stained with
201 Nile Red, imaged on a Leica M205 FCA stereoscope and recovered individually in a 12-well plate
202 whilst the SL of each fish was measured. Based on SL, fish were placed into groups with equal average
203 SL. Within groups, fish were randomly paired up and placed two fish per mesh insert in a 10L tank on
204 the recirculating system, allowing pairs of fish to be tracked through the experiment. The location of
205 each pair was randomly rotated daily to minimise tank location-effects. Fish assigned to the high-fat
206 diet group were immersed in 5% chicken egg yolk for two hours daily over the course of 14 days (16).
207 Control fish were placed in fresh system water for two hours daily. Both control and high-fat groups
208 received an additional two feeds throughout the day.

209

210 Image-based adipose morphology profiling in zebrafish

211 For each Nile Red-stained juvenile zebrafish, we took two images on a Leica M205 FCA fluorescence
212 stereomicroscope with a 1x objective: a whole animal image to allow us to measure total adiposity
213 and standard length (SL), and a higher magnification image of the lateral subcutaneous adipose tissue
214 (LSAT) along the zebrafish flank (hereafter referred to just as subcutaneous adipose or SAT). Images
215 were always taken of the right side of the fish, as zebrafish adipose shows left-right asymmetry, with
216 the right side containing the majority of pancreatic adipose. Images were first processed in
217 Fiji/ImageJ and the 'Clear Outside' function was used to reduce image size and focus on the SAT area
218 of interest or wider zebrafish. LD SAT images were either imported to Cellpose v2.2 and segmented
219 using the 'cyto' model (33), or segmented in Napari using the SAMCell plugin and the samcell-cyto-
220 large pre-trained model. Automated segmentations were assessed and manually adjusted to correct
221 errors. Segmented masks and object outlines were imported to Fiji/ImageJ where xy coordinates for
222 each segmented LD along with LD measurements were taken (including Feret's diameter for LD size).
223 ImageJ macros used for the importation of Cellpose masks and measurement of xy coordinates are
224 available at https://github.com/jeminchin/zebrafish_adipose_morphology_screen. Total adipose
225 area and SAT area were segmented using Ilastik software as previously described (34). Standard
226 length was measured using the line tool in Fiji/ImageJ.

227

228 Morphology value calculation

229 To quantify hyperplastic/hypertrophic adipose morphology we followed methodology from (35).
230 Briefly, for a given total SAT area, we modelled the expected mean LD diameter using a generalised
231 additive model (GAM):

232 $$Feret \sim s(\log(AreaSum))$$

233 where Feret is the mean LD Feret diameter, AreaSum is the total SAT area, and s denotes a penalised
234 thin-plate regression spline fitted using the mgcv package in R. The GAM was fitted, for each gene,
235 to all control (Cas9-only injected) fish pooled across experiments. Morphology value was calculated
236 at the individual-fish level as the deviation of the observed mean Feret diameter from the GAM-
237 predicted value. Positive deviations indicate a hypertrophic phenotype (larger LDs than expected for
238 a given adipose depot size), while negative deviations indicate a hyperplastic phenotype (smaller,
239 more numerous LDs).

240

241 Statistical framework for multi-experiment comparisons

242 Genes were tested across multiple independent injection experiments (typically 2–3 experiments per
243 gene, see **Fig. 5**). Two genes (*aspa* and *lamb2*) had morphology data from only a single experiment
244 and were analysed separately without batch correction. For genes with data from ≥2 experiments,
245 we employed complementary statistical approaches to identify robust phenotypes while controlling
246 for batch effects.

247

248 Kolmogorov-Smirnov tests

249 To assess distributional differences in morphology values between mutants and controls, we
250 performed two-sample Kolmogorov-Smirnov (KS) tests:

251 Pooled KS test: Control and mutant data were pooled across all experiments. A GAM was fit to pooled
252 control data, and KS tests compared the distribution of control residuals to mutant deviations from
253 the control GAM.

254 Stratified KS test: To validate that effects were consistent within experiments (rather than driven by
255 batch differences), we performed KS tests within each experiment separately, fitting experiment-
256 specific GAMs to control data. Within-experiment p-values were combined using Fisher's method:

$$\chi^2 = -2 \sum_{\{i=1\}}^{\{k\}} ln(p_i)$$

where k is the number of experiments. The combined statistic follows a χ^2 distribution with 2k degrees of freedom under the null hypothesis. Weighted mean effect sizes were calculated across experiments, weighting by sample size.

Linear mixed models

To quantify effect sizes while accounting for batch variation, we fit linear mixed models (LMMs) with experiment as a random intercept using the lme4 package.

Intercept model (uniform shift):

$$\log(Feret) \sim \log(AreaSum) + Genotype + (1|Experiment)$$

This tests whether mutants have uniformly larger or smaller LDs across all adipose depot sizes.

Interaction model (size-dependent effect):

$$\log(Feret) \sim \log(AreaSum)\ x\ Genotype + (1|Experiment)$$

This tests whether the allometric scaling relationship between LD size and total adiposity differs between genotypes. A significant interaction indicates that the mutant phenotype magnitude depends on total adipose tissue size.

Effect sizes from the intercept model were back-transformed to percentage changes in Feret diameter: % change = (exp(β) − 1) × 100, where β is the genotype coefficient. 95% confidence intervals were calculated as (exp(β ± 1.96 × SE) − 1) × 100.

Multiple testing correction

Benjamini-Hochberg false discovery rate (FDR) correction was applied separately to: (i) pooled KS tests, (ii) stratified KS tests (Fisher's combined p-values), (iii) LMM intercept p-values, and (iv) LMM slope p-values. Adjusted p-values < 0.05 were considered significant.

Robustness criteria

Genes were classified as robust hits if they reached significance (adjusted $p < 0.05$) in both the stratified KS test and LMM intercept test. This dual criterion ensures that: (i) the distributional effect is consistent within experiments (not a batch artifact), and (ii) the mean shift is statistically significant after accounting for repeated measures.

Variance heterogeneity analysis

To test whether mutants showed altered phenotypic variance beyond mean shifts, we performed F-tests comparing the variance of morphology values between genotypes. For each gene, variance ratio was calculated as $\sigma^2(\text{mutant})/\sigma^2(\text{control})$. Higher-order distributional moments were calculated using the moments package in R: skewness (asymmetry of distribution) and excess kurtosis (tail weight relative to normal distribution). The percentage of observations exceeding 2 standard deviations from the mean ("tail percentage") was also calculated. P-values from F-tests were corrected using Benjamini-Hochberg FDR.

LMM robustness verification

To verify that LMM results were not artifacts of violated model assumptions, we performed sensitivity analyses using three alternative approaches:

Heteroscedastic LMM: Linear mixed models allowing different residual variances per genotype were fit using the nlme package, with variance structure specified as weights = varIdent(form = ~1|genotype).

Permutation test: Genotype labels were permuted 1,000 times within each experiment to generate a null distribution of genotype effects. Permutation p-values were calculated as the proportion of permuted effects exceeding the observed effect.

Welch's t-test: Two-sample t-tests with Welch-Satterthwaite degrees of freedom correction (not assuming equal variance) were performed on morphology residuals.

308 Results were classified by consensus: "ALL SIG" if all methods yielded $p < 0.05$, "ALL NS" if no methods
309 were significant, or "MIXED" if methods disagreed. Only genes with consistent significance across all
310 sensitivity methods were considered to have robust LMM estimates.

311

312 Single-experiment gene analysis

313 For *aspa* and *lamb2* (single experiment each for morphology), batch correction was not possible.
314 These genes were analysed using standard linear regression:

315 $$\log(Feret) \sim \log(AreaSum) + Genotype$$

316 KS tests were also performed. Results are reported without FDR correction and should be interpreted
317 as preliminary findings requiring validation.

318

319 Software and code availability

320 All analyses were performed in R (version 4.5.1) using the following packages: mgcv for GAM fitting,
321 lme4 and lmerTest for linear mixed models, nlme for heteroscedastic mixed models, and moments
322 for distributional statistics. Code and data are available as a reusable pipeline at
323 https://github.com/jeminchin/zebrafish_adipose_morphology_screen.

324

325 Results

326 Identification of 102 candidate human adipose morphology genes enriched in adipocyte
327 stem and progenitor cells

328 To identify candidate regulators of hyperplastic/hypertrophic adipose morphology, we leveraged
329 previously published bulk RNA-Seq data that reported 3,727 differentially expressed genes (DEGs) in
330 human subcutaneous adipose tissue (SAT) characterised by either large or small adipocytes (**Fig. 1;**
331 **Suppl. Table 1**) (27). We reasoned these DEGs may contribute to defining hypertrophic or
332 hyperplastic adipose phenotypes. As the RNA-Seq was performed on whole SAT - comprising a
333 heterogeneous mix of cell types - we next asked which adipose-resident cell populations
334 preferentially express these morphology-associated genes. To address this, we clustered the 3,727

335 candidate genes based on their relative expression across 16 human white adipose tissue (WAT) cell
336 types, using published single-cell transcriptomic data (**Fig. 1; Suppl. Fig. 1**) (28). As expected, the
337 largest subset of morphology DEGs (n = 730) was enriched in mature adipocytes, consistent with
338 central roles for adipocytes in defining overall adipose morphology (**Suppl. Fig. 1**). Notably, we also
339 identified 102 DEGs enriched in adipose stem and progenitor cells (ASPCs) (**Fig. 1; Suppl. Fig. 1; Suppl.**
340 **Table 2**). Given prior evidence that ASPC abundance and differentiation rate can influence adipose
341 tissue expansion and morphology (36,37), we hypothesised that these genes may function within
342 ASPCs to regulate or establish adipose morphology.

343

344 Analysis of candidate human adipose morphology genes using GWAS and cardiometabolic 345 trait associations

346 Prior to functional analysis, we first explored genetic and cardiometabolic features of the 102
347 candidate genes. As an initial step, we examined overlap with BMI- and WHR-associated GWAS
348 genes, and found that 16 of the candidate morphology genes were also BMI GWAS genes (*TNRC6B*,
349 *LRMDA*, *PRRX1*, *TSHZ2*, *PTPRD*, *PARD3*, *ADH1B*, *TBX15*, *MAGI2*, *RTL8A*, *CAST*, *BNC2*, *RERE*, *PTPRG*,
350 *ADAMTSL1* and *C1QBP*) and one gene, *HOXC4*, overlapped with WHR-associated loci; however,
351 Fisher's exact test indicated these overlaps were not significantly enriched (**Suppl. Fig. 2**). We next
352 clustered candidate genes based on their SAT expression correlations with 23 cardiometabolic traits
353 from the METSIM study (29). This revealed two distinct gene–trait signatures: one associated with a
354 "healthy" metabolic profile - characterised by higher hip circumference, fat-free mass, HDL-C, Muscle
355 Insulin Sensitivity Index (MISI) and adiponectin levels, alongside lower BMI, WHR, total fatty acids,
356 triacylglycerides, Insulin and HOMA-B - and another with an "unhealthy" profile, showing the
357 opposite trait pattern (**Suppl. Fig. 2**). Notably, genes associated with both hypertrophic and
358 hyperplastic adipose morphology were found across both signatures (**Suppl. Fig. 2**), suggesting that
359 these morphological phenotypes are not strictly aligned with traditional markers of metabolic health.

360

361 Enrichment of cell differentiation and developmental genes among adipose morphology 362 candidates

363 To explore functional themes within our gene set, we performed enrichment analysis to identify
364 overrepresented biological processes. This analysis revealed that 54 of the 102 ASPC-enriched genes
365 were significantly associated with Gene Ontology (GO) terms related to cell differentiation
366 (GO:0030154) and tissue development (GO:0048869, GO:0009888, GO:0032502) (**Figs. 1, 2A,B &**
367 **Suppl. Table 3**). Reasoning that they may play key roles in ASPC differentiation and/or the patterning
368 of adipose tissue, we prioritised this subset of 54 genes for further analysis. To refine this list, we
369 applied two complementary strategies. First, we ranked genes by their sequence conservation
370 between humans and zebrafish (**Fig. 2D**). Second, we assessed scRNA-Seq expression dynamics
371 during progenitor differentiation to adipocytes (38) (**Figs. 2D–F**). From this, we shortlisted 25 highly
372 conserved genes that were predominantly expressed in either progenitors from undifferentiated
373 samples, or within multipotent progenitors that persist following differentiation (*MGP+* SWAT cells)
374 (**Figs. 2D–F & Table 1).** This final set included genes with established roles in adipocyte progenitors –
375 such as *PRRX1* (H. Liu et al., 2022), *TBX15* (Pan et al., 2021), and *IRX1* (Han, 2022) - though their
376 specific contributions to adipose morphology have not yet been characterised.

377

378 An image-based pipeline to quantify lipid droplet size, number and spatial patterning in 379 zebrafish subcutaneous adipose

380 To investigate the function of the candidate morphology genes, we developed an image-based
381 phenotyping pipeline in zebrafish. Building on previous studies where Nile Red fluorescence was used
382 to quantify whole-animal adiposity and perform targeted CRISPR screens for regulators of total body
383 fat (16,26), we refined this approach to capture not only global adiposity data but also high-resolution
384 images of Nile Red-positive LDs. This enabled detailed quantification of LD size, number and spatial
385 patterning within zebrafish SAT (**Fig. 3A-D**). High-magnification images were acquired with a pixel
386 size between 1-2 μm^2 allowing individual LDs to be clearly resolved within zebrafish SAT (**Fig. 3A–D**).
387 Although very small LDs within multilocular adipocytes fall below our detection threshold, this
388 resolution reliably captures the larger LDs characteristic of mature adipocytes (**Fig. 3A-D**). Using this
389 pipeline, we characterised SAT development in 107 wild-type zebrafish from three independent
390 clutches (**Fig. 1E-G**). Representative LD masks illustrating the morphological progression of SAT
391 expansion are shown in **Fig. 3E**. Consistent with previous observations, LDs are first deposited at the
392 anterior end of the adipose depot and new LDs are added in both posterior and dorsoventral

393 directions (**Fig. 3E**). To spatially track this progression, we annotated the most anterior LD and defined
394 successive 200 µm strata extending posteriorly from this reference point (**Fig. 3E**). This stratification
395 enabled comparisons of LD morphology and number at anatomically and developmentally equivalent
396 positions across individuals. As zebrafish grew from 7 to 12 mm standard length (SL), we observed
397 limited increases in LD number within the anterior-most stratum (stratum 1) (**Fig. 3E & F**). Instead,
398 new LDs accumulated in more posterior regions, particularly in strata 3 and 4, which exhibited the
399 greatest LD number and overall growth (**Figs. 3E & F**). Concurrently, LDs increased in size, reaching
400 an average diameter of ~65 µm by 11–12 mm SL (**Fig. 3E & G**). Notably, posterior strata - containing
401 more recently formed LDs - appeared to be in the process of enlarging toward this consistent size
402 benchmark (**Fig. 3E & G**). Together, these findings show that during these relatively young juvenile
403 stages, LDs expand rapidly in size but ultimately stabilise at an average diameter of ~65 µm, reflecting
404 a potential upper limit of LD growth at this developmental stage.

405

406 Quantification of adipose morphology in juvenile zebrafish

407 As LD size, number and spatial dynamics can be robustly captured in juvenile zebrafish, we next
408 developed methodology to quantify adipose morphology – specifically hyperplastic versus
409 hypertrophic patterns – in a format scalable for CRISPR-based screening. Our approach was
410 conceptually based on previously described methods for assessing human adipose morphology (35).
411 To establish a baseline, we quantified SAT LD number and size within 194 wild-type fish (including
412 the 107 animals analysed in **Fig. 3**). We observed a strong curvilinear relationship between mean LD
413 diameter and the total depot size (R^2 = 0.85) (**Fig. 4A**). This relationship also held true for other LD
414 size metrics (including area and perimeter), further suggesting that as the zebrafish SAT expands, LDs
415 initially grow rapidly in size but then plateau as they reach a steady-state size and hypertrophic
416 growth slows relative to the overall size of the depot. Following the strategy of Arner et al (2010), we
417 calculated a 'morphology value' for each individual based on the deviation of each fish from the fitted
418 curve (**Fig. 4B**). Morphology values were normally distributed around zero, with approximately equal
419 proportions of individuals exhibiting hyperplastic (negative deviation) or hypertrophic (positive
420 deviation) SAT (**Fig. 4B**). Notably, morphology values were inversely correlated with LD number (p =
421 3.9×10^{-6}), such that hypertrophic individuals had fewer, larger LDs while hyperplastic individuals had

422 more numerous, smaller LDs (**Fig. 4C**). Together, these data show that morphology values can be
423 applied to zebrafish SAT and used to quantify hyperplastic/hypertrophic patterning.

424

425 Morphology values can be used to assess differences in F0 zebrafish CRISPR mutants

426 We next tested whether this metric could detect known regulators of adipose morphology. As a
427 positive control, we targeted *growth hormone 1* (*gh1)* using established F0 CRISPR mutant
428 methodology. Consistent with previous findings that *gh1* mutants display hypertrophic SAT LDs (39),
429 *gh1* F0 CRISPR mutants displayed significantly larger LDs and an upward shift in morphology values
430 (p = 0.04) (**Suppl. Fig. 3**). Notably, this effect was detected in only nine *gh1*-targeted fish,
431 corresponding to a large effect size (Cohen's d = 1.06) (**Suppl. Fig. 3**). Power analysis based on this
432 dataset indicated that similar effects could be detected with 80% power using as few as 11 fish.
433 Moreover, detecting medium-sized effects (Cohen's d = 0.6-0.7) would require only 23-31 mutant
434 fish. Together, these results demonstrate that image-based profiling of adipose morphology is a
435 sensitive and scalable approach for in vivo genetic screens aimed at identifying regulators of
436 hyperplastic and hypertrophic adipose growth.

437

438 A targeted CRISPR screen identified three genes that induce hypertrophic morphology in
439 subcutaneous adipose

440 Following validation of our morphology quantification approach using *gh1*, we applied the same F0
441 CRISPR methodology and image-based pipeline to functionally assess all 25 conserved candidate
442 genes identified from human adipose tissue datasets. In total, we screened 1,371 juvenile zebrafish
443 comprising 738 Cas9-only controls and 633 gene-targeted mutants across 2-3 independent
444 experimental replicates per gene (**Fig. 5A-C & Table 1**). Two targets, *phb* and *rerea*, were lethal prior
445 to 5 dpf and therefore excluded from morphological analysis. Of the remaining 23 genes, none
446 showed significant effects on standard length after controlling for batch effects, indicating that
447 CRISPR targeting did not cause generalised growth defects (**Fig. 5D**). One gene (*kazna*) showed
448 significantly increased total adiposity (**Fig. 5E**).

449 To quantify SAT morphology and classify hyperplastic or hypertrophic profiles, we applied two
450 complementary statistical approaches. First, we calculated morphology values for each fish and

451 compared mutant versus control morphology value distributions using the Kolmogorov-Smirnov (KS)
452 test. This non-parametric test does not assume a specific distribution and is sensitive to shape-based
453 distributional changes. To ensure effects were consistent across experimental batches rather than
454 driven by between-experiment variability, we performed both pooled KS tests (combining data
455 across all experiments) and stratified KS tests (testing within each experiment separately, then
456 combining p-values using Fisher's method). Second, we applied linear mixed-models (LMMs) to
457 evaluate the relationship between LD size and total SAT area, whilst accounting for replicate-specific
458 variability. The LMMs allowed us to test whether LDs scaled normally with tissue size (slope) or
459 differed in size at any given adipose area (intercept). After correcting for multiple tests using the
460 Benjamini-Hochberg procedure, we identified three genes with robust hypertrophic morphology
461 phenotypes validated by both stratified KS tests (which control for batch effects by testing within
462 each experiment) and linear mixed models: *txnipa* (+19.9% increase in LD diameter, stratified KS adj.p
463 = 1.41×10−4, LMM adj.p = 1.63×10−4), *mmp14b* (+15.8%, stratified KS adj.p = 0.005, LMM adj.p =
464 1.93×10−4), and *foxp1b* (+17.0%, stratified KS adj.p = 0.019, LMM adj.p = 0.049) (**Table 1 & Fig. 5**).
465 Two genes (*tmem115* and *tbx15*) showed significant distributional shifts in stratified KS tests (adj.p =
466 0.019 for both) but non-significant LMM intercept effects, suggesting altered variance or size-
467 dependent phenotypes rather than uniform shifts in LD size (**Table 1**). Indeed, *tbx15* mutants
468 displayed a significantly steeper size-scaling slope (+0.107, adj.p = 0.026), indicating that any
469 hypertrophic tendency is more pronounced in larger fish (**Table 1**). Three additional genes showed
470 nominally significant effects in pooled KS tests prior to FDR correction but were not validated by
471 stratified within-experiment analysis: *ptprdb* (hypertrophic, +18.5%), *ptenb* (hyperplastic, −7.9%),
472 and *srpx* (hyperplastic, −0.9%) (**Table 1**). These represent suggestive hits that may warrant further
473 investigation in stable mutant lines. Together, these findings demonstrate image-based profiling is
474 an effective and scalable approach for identifying regulators of adipose morphology.

475

Gene	**Reps**	**n (ctrl/mut)**	**KS test**			**LMM**		**Direction**	**Power (d = 0.8)**
			Effect (μm)	**Pooled (FDR adj. p value)**	**Stratified (FDR adj. p value)**	**Effect (%)**	**FDR adj. p value**		

txnipa	3	45/30	+4.6	0.066	**1.41e-04**	+19.9%	**1.63e-04**	Hypertrophic	92%
mmp14b	2	34/30	+5.4	**0.002**	**0.005**	+15.8%	**1.93e-04**	Hypertrophic	88%
foxp1b	2	42/45	+8.8	0.064	**0.019**	+17.0%	**0.049**	Hypertrophic	96%
ptprdb	2	35/24	+4.0	0.080	0.057	+18.5%	0.087	Hypertrophic	84%
cxcl14	2	27/24	-4.4	0.522	0.077	-8.7%	0.348	Hyperplastic	80%
prrx1b	3	65/60	-3.5	0.178	0.077	-5.9%	0.358	Hyperplastic	99%
ptenb	2	27/25	-4.7	0.054	0.077	-7.9%	0.411	Hyperplastic	81%
pid1	2	27/26	-2.7	0.869	0.204	-6.5%	0.565	Hyperplastic	81%
nav3	3	49/42	-2.4	0.194	0.562	-6.1%	0.650	Hyperplastic	96%
sdk1a	2	29/25	+0.6	0.869	0.482	+7.6%	0.694	Hypertrophic	82%
runx1t1	2	29/22	+1.1	0.706	0.795	+7.6%	0.736	Hypertrophic	79%
sparc	2	24/23	-2.1	0.286	0.553	-7.1%	0.736	Hyperplastic	77%
kazna	2	36/23	-3.1	0.706	0.148	-4.7%	0.759	Hyperplastic	84%
tmem115	2	27/29	-3.1	0.488	**0.019**	-3.8%	0.759	Hyperplastic	84%
cd81a	2	24/26	+0.0	0.862	0.064	-5.0%	0.759	Hypertrophic	79%
lrmda	2	27/22	-0.4	0.527	0.077	-2.7%	0.778	Hyperplastic	78%
tbx15	3	37/26	+3.4	0.706	**0.019**	+3.7%	0.778	Hypertrophic	87%
cacnb4a	2	29/27	+0.9	0.706	0.852	+2.6%	0.804	Hypertrophic	84%
pard3ab	2	36/32	-1.5	0.869	0.750	+2.1%	0.804	Hypertrophic	90%
ptprga	2	35/35	-1.4	0.269	0.077	-1.6%	0.804	Hyperplastic	91%
srpx	2	36/20	-5.7	0.155	0.204	-0.9%	0.836	Hyperplastic	80%

Table 1. Zebrafish gene targets and adipose morphology statistics. Adjusted p values after Benjamini-Hochberg FDR correction for 21 statistical tests. KS = Kolmogorov-Smirnov test. LMM = linear mixed model with experiment as random effect. Values in bold indicate statistical significance. Gene names in bold indicate robust phenotypes (significant in both stratified KS and LMM). Stratified KS tests were performed within each experiment and combined using Fisher's method. Genes with only one replicate (*aspa*, *lamb2*) or which showed lethality (*phb*, *rerea*) are not included in this table.

A hypertrophic growth bias of subcutaneous adipose in *foxp1b* and double *foxp1a;foxp1b* zebrafish mutants

485 Notably, targeting *foxp1b* (one of two zebrafish *foxp1* genes) induced hypertrophic SAT morphology
486 (**Fig. 5**). Foxp1 is required for maintaining undifferentiated and self-renewing stem and progenitor
487 cells in multiple tissue compartments (40–44). Further, in mouse, Foxp1 inhibits brown adipogenesis
488 and browning of white adipocytes (45). However, roles for Foxp1 in establishing
489 hyperplastic/hypertrophic morphology of adipose is unknown. To further study the role of Foxp1, we
490 generated new loss-of-function alleles for both *foxp1* genes (*foxp1a* and *foxp1b*) in zebrafish (**Fig.**
491 **6A**). We targeted the highly conserved Forkhead domain (FHD) (**Fig. 6B**), which is essential for DNA
492 binding and therefore Foxp1 transcriptional activity (46,47) (**Fig. 6B**). We generated two alleles –
493 *foxp1a*^{ed116} and *foxp1b*^{ed125} – which each contained a frameshift and premature stop codon within
494 the FHD (**Fig. 6B**). qRT-PCR revealed reduced *foxp1a* or *foxp1b* mRNA in the respective single mutants,
495 with no apparent mRNA upregulation of the paralogous *foxp1* gene, or other members of the Foxp
496 family (**Suppl. Fig. 4**). Western blots revealed a significant reduction of Foxp1 protein in each of the
497 single mutants, and in *foxp1a;foxp1b* double mutants suggesting severe loss-of-function alleles (**Fig.**
498 **6C & Suppl. Fig. 4**). At approximately one-month of age (~10 mm SL), *foxp1b*^{ed125} and double
499 *foxp1a;foxp1b* mutants were significantly smaller than either wild-type control or *foxp1a*^{ed116} fish
500 (**Fig. 6E**). Analysis of baseline lipid storage using Nile Red revealed that *foxp1a;foxp1b* double mutants
501 had significantly lower normalised adipose area than controls, while *foxp1b* single mutants showed
502 a non-significant trend (**Fig. 6D,F**). Critically, despite their smaller body size, both *foxp1b*^{ed125} and
503 *foxp1a;foxp1b* mutants had significantly larger LDs characteristic of hypertrophic morphology (**Fig.**
504 **6G).** This dissociation between body size (smaller) and LD size (larger) argues against a simple
505 developmental delay: if these mutants were merely developmentally delayed, we would expect
506 smaller fish to have smaller LDs, as observed during normal development (**Fig. 3G**). Instead, *foxp1b*
507 mutants seem to display fundamentally altered adipose growth properties. Analysis of blood
508 metabolites revealed *foxp1a;foxp1b* double mutants were hyperglycaemic (**Suppl. Fig. 5**), and
509 strikingly, in *foxp1a;foxp1b* double mutants there was increased lipid accumulation in the liver (**Fig.**
510 **6D & Suppl. Fig. 5D**). At adulthood, fish size and lipid storage within adipose in *foxp1a;foxp1b* double
511 mutants had largely caught up with wild-type control fish (adiposity at ~80% of wild-type levels)
512 (**Suppl. Fig. 6**). These findings show that stable *foxp1b* mutants have hypertrophic adipose along with
513 metabolic dysfunction.

514

515 ## Spatial analysis reveals profoundly blunted hypertrophic responses to high-fat diet in
516 ## *foxp1b* mutants

517 Our previous analyses showed that *foxp1b* mutants display a bias toward hypertrophic growth during
518 developmental expansion of SAT. To determine whether this bias impacts the adipose response to
519 dietary challenge, we subjected *foxp1a* and *foxp1b* mutants to a two-week high-fat diet (HFD), a
520 condition previously shown to induce SAT expansion (16). All *foxp1* mutant genotypes exhibited
521 reduced overall HFD-induced adipose expansion compared to control fish, indicating a general
522 impairment in expansion capacity (**Suppl. Fig. 7**). To characterise the HFD response, we performed
523 spatial analysis by binning the anterior-posterior (AP) axis into 200 µm strata, enabling comparison
524 of LD morphology at anatomically equivalent positions (**Fig. 6H-M**). Using paired analysis (same fish
525 imaged on control diet at 35 dpf and after 14 days HFD at 49 dpf) with linear mixed-effects models,
526 we quantified diet effects across all strata. First, we confirmed that on a control diet, *foxp1b* mutants
527 had significantly larger LDs than wild-type across strata 1–5 (ranging from +22.2 µm in stratum 1 to
528 +17.8 µm in stratum 5; all FDR-adjusted $p < 0.05$; **Fig. 6I**). By contrast, *foxp1a* mutants showed no
529 baseline hypertrophy at any stratum (all $p > 0.10$; **Suppl. Figs. 8 & 9**). Second, spatial analysis revealed
530 that *foxp1b* mutants show profoundly blunted hypertrophic responses to HFD. In wild-type fish, HFD
531 induced robust LD hypertrophy across all 15 strata (range: +17.7 to +28.1 µm; all FDR-adjusted $p <$
532 0.025; **Fig. 6J**). However, *foxp1b* mutants showed a strikingly different pattern: in anterior/oldest
533 strata (1–5), mutants showed significant but attenuated HFD responses (+7.7 to +12.2 µm; ~57%
534 weaker than wild-type; FDR-adjusted $p < 0.05$ for strata 3–5), while in posterior/newer strata (7–15),
535 there was essentially no hypertrophic response (effect sizes declining from +6.8 µm to +0.4 µm; all
536 FDR-adjusted $p > 0.068$; **Fig. 6J**). Overall, averaging across all strata, wild-type LDs increased by +24.4
537 µm in response to HFD ($p < 0.0001$), whereas *foxp1b* mutant LDs increased by only +7.7 µm ($p =$
538 0.020) - representing a 68% reduction in hypertrophic capacity (**Fig. 6K**). *foxp1a* mutants had no
539 baseline hypertrophy on control diet (all strata $p > 0.10$; **Fig. 6L**), but still exhibited significantly
540 blunted HFD responses (~35% reduction compared to wild-type; $p = 0.023$; **Fig. 6M**), demonstrating
541 that an impaired adaptive response can occur independently of baseline LD size. Interestingly, *foxp1a*
542 mutants also lost the spatial gradient of HFD responsiveness observed in wild-type fish (uniform
543 +14.4 µm across all strata vs wild-type range of +16.6 to +26.4 µm anteriorly to posteriorly),
544 suggesting Foxp1a may regulate spatial coordination within the tissue. Together, these spatial
545 analyses reveal that *foxp1b* mutants have intrinsically impaired capacity for diet-induced

546 hypertrophic remodelling, while *foxp1a* mutants show a distinct phenotype affecting the magnitude
547 and spatial patterning of adaptive responses. These findings demonstrate that Foxp1 paralogues play
548 non-redundant roles in regulating both constitutive adipose morphology and adaptive responses to
549 nutritional challenge.

550

551 ## Discussion

552 In this study, we (i) identified candidate human genes implicated in hypertrophic and hyperplastic
553 adipose morphology, (ii) established an image-based profiling method for assessing adipose
554 morphology in zebrafish, (iii) conducted an in vivo CRISPR screen to functionally evaluate the roles of
555 25 candidate genes with rigorous statistical validation, (iv) identified three genes that induce
556 hypertrophic adipose morphology, (v) generated stable *foxp1a* and *foxp1b* zebrafish mutant lines
557 that recapitulate phenotypes observed in the F0 CRISPR experiments and revealed paralogue-specific
558 roles in adipose biology, and (vi) discovered through spatial analysis that *foxp1b* mutants have
559 intrinsically impaired capacity for diet-induced hypertrophic remodelling. Together, this work
560 demonstrates a scalable, rigorous screening platform to identify regulators of adipose morphology
561 with clear translational potential.

562

563 **Candidate gene identification from human data**

564 We employed a multi-step process to identify candidate morphology genes from human
565 transcriptomic data. As GWAS for adipose morphology has only been conducted in relatively small
566 cohorts (48,49), we instead used published data identifying DEGs enriched in SAT characterised by
567 large or small adipocytes (27). Clustering of the morphology DEG expression correlations with
568 cardiometabolic traits separated genes into 'healthy' and 'unhealthy' profiles (**Suppl. Fig. 2**); genes
569 associated with larger adipocytes generally aligned with adverse metabolic traits such as increased
570 BMI and WHR in accordance with adipocyte size increasing with BMI (50). However, this pattern was
571 not absolute—some candidates diverged from this axis (**Suppl. Fig. 2**), representing potentially
572 interesting regulators of adipose morphology that are uncoupled from traditional metabolic or
573 disease states. We focussed on candidate genes highly expressed in adipocyte stem and progenitor
574 cells (ASPCs), reasoning that progenitor function influences both hyperplastic potential and overall

575 remodelling capacity. However, we note that adipose remodelling is likely determined by multiple
576 cell types beyond progenitors, including the adipose microenvironment (51,52).

577

578 **An image-based platform for profiling adipose morphology**

579 We established a rapid, scalable, stereomicroscope-based imaging pipeline for profiling zebrafish
580 adipose morphology. Our imaging resolution was sufficient to detect large LDs but not smaller
581 secondary LDs found in zebrafish adipocytes (52), a phenomenon also observed in mouse adipocytes
582 (53). Nevertheless, our methodology reliably captured primary LDs and allowed us to use LD size as
583 a proxy for overall adipocyte size. We adapted the morphology value framework developed by the
584 Arner lab for human adipose (35), and observed strikingly similar relationships in zebrafish SAT,
585 including a curvilinear relationship between LD size and depot size and an inverse correlation
586 between LD number and LD size. These parallels suggest that the fundamental growth dynamics of
587 zebrafish adipose are conserved with mammals, supporting zebrafish as a relevant model for
588 studying adipose biology.

589

590 **Statistical validation and batch effect control**

591 A key advance of our platform is the implementation of rigorous statistical validation to control for
592 batch effects - a common source of false positives in genetic screens. We employed two
593 complementary approaches: Kolmogorov–Smirnov (KS) tests to compare morphology value
594 distributions, and linear mixed models (LMMs) to assess LD size while accounting for experimental
595 batch as a random effect. Critically, we performed both pooled KS tests (combining data across
596 experiments) and stratified KS tests (testing within each experiment separately, then combining p-
597 values using Fisher's method). This stratified approach validates that phenotypic effects are
598 reproducible within independent experiments rather than driven by between-batch variability.
599 Genes were considered robust hits only if significant in both stratified KS and LMM analyses after
600 FDR correction—a conservative threshold that substantially reduces false discovery risk. Using these
601 criteria, we identified three genes (*txnipa*, *mmp14b*, *foxp1b*) as robust hypertrophic hits. Three
602 additional genes (*ptprdb*, *ptenb*, *srpx*) showed suggestive effects in pooled analyses but were not
603 validated by stratified tests, indicating potential batch artifacts or weaker effects requiring larger

604 sample sizes. Two genes (*tbx15*, *tmem115*) showed significant distributional shifts in stratified KS
605 without corresponding LMM intercept effects; notably, *tbx15* displayed a significant slope effect,
606 indicating size-dependent rather than uniform phenotypes. This statistical framework - combining
607 distribution-sensitive tests with mixed models and stratified validation - provides a template for
608 future high-throughput screens where batch effects are unavoidable.

609

610 **Functional insights from screen hits**

611 *Txnipa (txnipa)* F0 CRISPR mutants displayed hypertrophic morphology. TXNIP (Thioredoxin-
612 Interacting Protein) is a well-characterised regulator of oxidative stress, metabolism, and
613 inflammation that binds and inhibits thioredoxin, leading to increased production of reactive oxygen
614 species and oxidative stress (54). TXNIP links nutrient sensing to inflammatory signalling by
615 responding to glucose and regulating NLRP3 inflammasome activation (54). The ROS/TXNIP/NLRP3
616 pathway impairs insulin signalling, a major driver of adipogenesis and hyperplastic adipose growth
617 (55), potentially explaining why *txnipa* loss biases toward hypertrophy. Additionally, vitamin D
618 increases TXNIP expression (56), and plays a major role in energy storage in zebrafish (57), suggesting
619 nutrient-sensing pathways may coordinate morphological outcomes.

620 *Mmp14b* F0 zebrafish mutants also exhibited hypertrophic adipose. MMP14 (Matrix
621 Metallopeptidase 14) is a pericellular collagenase and plays a key role in ECM remodelling. In mice,
622 MMP14 deficiency stiffens the adipose matrix and restricts expansion, resulting in smaller adipocytes
623 (58), while overexpression of Mmp14 increased the size of adipocytes (59). Our zebrafish findings –
624 hypertrophy upon mmp14b loss – appear to contrast with these mouse phenotypes and warrant
625 further investigation. Notably, zebrafish possess two *mmp14* paralogues, therefore functional
626 redundancy or divergence between paralogues may underlie species-specific differences. Future
627 studies targeting both paralogues simultaneously would clarify this.

628

629 **Paralogue selection: strengths and limitations**

630 Our screen targeted single paralogues based on DIOPT orthology scores, selecting the zebrafish gene
631 with highest predicted orthology to each human candidate. This approach has important limitations:
632 orthology scores predict sequence conservation but not necessarily functional equivalence, meaning

633 the "most orthologous" paralogue may not carry the relevant adipose function. Indeed, our three
634 candidate hit genes have multiple zebrafish paralogues (FOXP1, TXNIP, MMP14), and testing only one
635 paralogue means we may have missed genuine hits where the alternative paralogue is functionally
636 relevant. Our Foxp1 findings both validate this approach and reveal its limitations. The higher-scoring
637 paralogue *foxp1b* (DIOPT score 13/19) showed the more severe baseline phenotype, consistent with
638 our prioritisation. However, *foxp1a* (DIOPT score 5/19), tested subsequently, revealed a distinct and
639 biologically significant phenotype affecting spatial patterning of HFD responses - a finding that would
640 have been missed had we not pursued secondary validation. For future screens where
641 comprehensive hit identification is the goal, multiplexed F0 targeting of all paralogues may be
642 valuable (67), though this approach may complicate interpretation of paralogue-specific phenotypes.

643

644 **Non-redundant roles for Foxp1 paralogues in adipose biology**

645 *Foxp1* is known to maintain stem and progenitor populations across multiple tissues including the
646 hair follicle, haematopoietic niche, mammary gland, and cerebral cortex (40,41,43,44). We
647 hypothesised that Foxp1 may be required in adipose progenitors for hyperplastic growth, with its
648 loss resulting in compensatory hypertrophy. *Foxp1b* mutants displayed constitutive hypertrophy at
649 baseline - smaller fish with paradoxically larger LDs - along with a reduced hypertrophic response to
650 HFD together with reduced adipose coverage, hyperglycaemia, and hepatic steatosis in double
651 mutants. In contrast, *foxp1a* mutants showed no baseline morphological defects but also exhibited
652 impaired adaptive responses to HFD and a breakdown in anterior-posterior patterning in the adipose
653 tissue. These data suggest both *foxp1* paralogues regulate adaptive responses to HFD, but also
654 regulate distinct aspects of adipose biology: Foxp1b controlling constitutive morphology and Foxp1a
655 regulating spatial patterning.

656

657 **Impaired adaptive capacity rather than developmental ceiling**

658 A key finding from our spatial analysis is that *foxp1b* mutants have intrinsically impaired capacity for
659 diet-induced hypertrophy, rather than having reached a developmental size limit. Several
660 observations support this conclusion. First, the blunted HFD response in *foxp1b* mutants extended
661 throughout the entire anterior-posterior axis (68% overall reduction), including posterior regions

662 containing smaller, newer LDs. If anterior adipocytes had simply reached maximum size, we would
663 expect normal responses posteriorly - but instead we observed complete loss of response in posterior
664 strata. Second, and most strikingly, wild-type LDs on HFD actually surpassed *foxp1b* mutant sizes in
665 posterior strata, demonstrating that these sizes are not developmentally limiting. Third, *foxp1a*
666 mutants showed blunted HFD responses (~35% reduction) despite having no baseline hypertrophy,
667 proving that impaired adaptive capacity can occur independently of baseline LD size. These findings
668 have important implications. They suggest that both *foxp1a* and *foxp1b* mutants may fail to perceive
669 or respond to HFD-induced molecular cues, potentially implicating Foxp1 in metabolic sensing
670 pathways (66). The distinct *foxp1a* phenotype - loss of spatial gradients in HFD responsiveness -
671 suggests this paralogue may coordinate regional heterogeneity within adipose tissue. Testing
672 whether other hypertrophic mutants identified in our screen (*txnipa*, *mmp14b*) also show impaired
673 adaptive responses would determine whether this reflects a general principle linking developmental
674 morphology to later plasticity.

675

676 **Comparison with mammalian Foxp1 studies**

677 In mouse, adipose-specific Foxp1 deletion increases browning of white adipose tissue and enhances
678 thermogenesis, protecting against diet-induced obesity (45). Our zebrafish findings – where whole-
679 organism *foxp1b* loss causes metabolic dysfunction rather than protection – appear contradictory
680 but likely reflect important experimental differences. First, Liu et al. studied browning-prone inguinal
681 WAT, whereas zebrafish adipose, as in an ectotherm, is not traditionally considered thermogenic –
682 though recent evidence shows zebrafish epicardial adipose can be thermogenic (15). In browning-
683 resistant depots, more commonly observed in humans, Foxp1 loss might produce phenotypes more
684 similar to our zebrafish findings. Second, our whole-organism mutants also lack hepatic Foxp1 which
685 regulates gluconeogenesis (65); the metabolic dysfunction we observe may reflect hepatic rather
686 than adipose-autonomous effects. Tissue-specific approaches in zebrafish would help distinguish
687 these contributions.

688

689 **Platform scalability and translational potential**

690 Our screening platform offers several advantages for systematic functional genomics. First, it is highly
691 scalable: we screened 1,371 fish across 25 genes with sufficient statistical power (>80% for large
692 effects) in each case. The imaging pipeline requires only standard stereomicroscopy, and analysis is
693 fully automated. Second, it is modular: the same fish can be assessed for multiple phenotypes (body
694 size, total adiposity, morphology, spatial patterning), and the platform readily accommodates dietary
695 or pharmacological challenges. Third, results translate meaningfully to mammalian biology, as
696 demonstrated by the conservation of morphology value relationships. Compared to mammalian
697 screening platforms, zebrafish offer dramatically reduced costs and timelines while enabling whole-
698 organism assessment of gene function. However, limitations include the lack of tissue-specific genetic
699 tools comparable to Cre-lox systems, potential paralogue complications, and the possibility that
700 some mammalian adipose biology (particularly thermogenesis) may not be fully conserved.
701 Nevertheless, our identification of genes with established human disease relevance (*TXNIP*, *MMP14*,
702 *FOXP1*) demonstrates clear translational line-of-sight from zebrafish discoveries to human adipose
703 biology.

704

705 Acknowledgements

706 We thank Rosalyn Fong for help with initial zebrafish *foxp1* genotyping strategies, and David Duneau,
707 Will Cawthorn and Rob Semple for advice on modelling of adipose morphology. The work was funded
708 by a British Heart Foundation PhD Studentship awarded to RW, and a BBSRC grant (BB/X009467/1)
709 awarded to PT and JENM.

710

711 Author contributions

712 RW and PT performed experiments, RW, PT and JENM performed data analysis, PT and JENM wrote
713 the manuscript.

714 **REFERENCES**

715 1. Tandon P, Wafer R, Minchin JEN. Adipose morphology and metabolic disease. J Exp Biol. 2018 Mar
716 7;221(Pt Suppl 1):jeb164970.

717 2. Hagberg CE, Spalding KL. White adipocyte dysfunction and obesity-associated pathologies in humans. Nat
718 Rev Mol Cell Biol. 2024 Apr;25(4):270–89.

719 3. Vishvanath L, Gupta RK. Contribution of adipogenesis to healthy adipose tissue expansion in obesity. J
720 Clin Invest. 2019 Oct 1;129(10):4022–31.

721 4. Rydén M, Arner P. Cardiovascular risk score is linked to subcutaneous adipocyte size and lipid metabolism.
722 J Intern Med. 2017 Sep;282(3):220–8.

723 5. Acosta JR, Douagi I, Andersson DP, Bäckdahl J, Rydén M, Arner P, et al. Increased fat cell size: a major
724 phenotype of subcutaneous white adipose tissue in non-obese individuals with type 2 diabetes.
725 Diabetologia. 2016 Mar;59(3):560–70.

726 6. Weyer C, Foley JE, Bogardus C, Tataranni PA, Pratley RE. Enlarged subcutaneous abdominal adipocyte
727 size, but not obesity itself, predicts type II diabetes independent of insulin resistance. Diabetologia. 2000
728 Dec;43(12):1498–506.

729 7. Hoffstedt J, Arner E, Wahrenberg H, Andersson DP, Qvisth V, Löfgren P, et al. Regional impact of adipose
730 tissue morphology on the metabolic profile in morbid obesity. Diabetologia. 2010 Dec;53(12):2496–503.

731 8. Boden G, Cheung P, Mozzoli M, Fried SK. Effect of thiazolidinediones on glucose and fatty acid metabolism
732 in patients with type 2 diabetes. Metabolism. 2003 Jun;52(6):753–9.

733 9. Kim SM, Lun M, Wang M, Senyo SE, Guillermier C, Patwari P, et al. Loss of white adipose hyperplastic
734 potential is associated with enhanced susceptibility to insulin resistance. Cell Metab. 2014 Dec
735 2;20(6):1049–58.

736 10. Gao Z, Daquinag AC, Fussell C, Zhao Z, Dai Y, Rivera A, et al. Age-associated telomere attrition in adipocyte
737 progenitors predisposes to metabolic disease. Nat Metab. 2020 Dec;2(12):1482–97.

738 11. Muir LA, Neeley CK, Meyer KA, Baker NA, Brosius AM, Washabaugh AR, et al. Adipose tissue fibrosis,
739 hypertrophy, and hyperplasia: Correlations with diabetes in human obesity. Obesity . 2016
740 Mar;24(3):597–605.

741 12. Arner P, Arner E, Hammarstedt A, Smith U. Genetic predisposition for Type 2 diabetes, but not for
742 overweight/obesity, is associated with a restricted adipogenesis. PLoS One. 2011 Apr 12;6(4):e18284.

743 13. Flynn EJ 3rd, Trent CM, Rawls JF. Ontogeny and nutritional control of adipogenesis in zebrafish (Danio
744 rerio). J Lipid Res. 2009 Aug;50(8):1641–52.

745 14. Imrie D, Sadler KC. White adipose tissue development in zebrafish is regulated by both developmental
746 time and fish size. Dev Dyn. 2010 Nov;239(11):3013–23.

747 15. Morocho-Jaramillo P-A, Kotlar-Goldaper I, Zakarauskas-Seth BI, Purfürst B, Filosa A, Sawamiphak S. The
748 zebrafish heart harbors a thermogenic beige fat depot analog of human epicardial adipose tissue. Cell
749 Rep. 2024 Mar 26;43(3):113955.

750 16. Minchin JEN, Rawls JF. A classification system for zebrafish adipose tissues. Dis Model Mech. 2017 Jun
751 1;10(6):797–809.

752 17. Minchin JEN, Scahill CM, Staudt N, Busch-Nentwich EM, Rawls JF. Deep phenotyping in zebrafish reveals
753 genetic and diet-induced adiposity changes that may inform disease risk. J Lipid Res. 2018
754 Aug;59(8):1536–45.

755 18. Oka T, Nishimura Y, Zang L, Hirano M, Shimada Y, Wang Z, et al. Diet-induced obesity in zebrafish shares
756 common pathophysiological pathways with mammalian obesity. BMC Physiol. 2010 Oct 21;10(1):21.

757 19. Landgraf K, Schuster S, Meusel A, Garten A, Riemer T, Schleinitz D, et al. Short-term overfeeding of
758 zebrafish with normal or high-fat diet as a model for the development of metabolically healthy versus
759 unhealthy obesity. BMC Physiol. 2017 Mar 21;17(1):4.

760 20. Minchin JEN, Rawls JF. In vivo analysis of white adipose tissue in zebrafish. Methods Cell Biol.
761 2011;105:63–86.

762 21. Lumaquin D, Johns E, Montal E, Weiss JM, Ola D, Abuhashem A, et al. An in vivo reporter for tracking lipid
763 droplet dynamics in transparent zebrafish. Elife [Internet]. 2021 Jun 11;10. Available from:
764 https://pubmed.ncbi.nlm.nih.gov/34114952/

765 22. Wilson MH, Ekker SC, Farber SA. Imaging cytoplasmic lipid droplets in vivo with fluorescent perilipin 2
766 and perilipin 3 knock-in zebrafish. Elife [Internet]. 2021 Aug 13;10. Available from:
767 https://pubmed.ncbi.nlm.nih.gov/34387191/

768 23. Lepanto P, Levin-Ferreyra F, Koziol U, Malacrida L, Badano JL. Insights into in vivo adipocyte
769 differentiation through cell-specific labeling in zebrafish. Biol Open [Internet]. 2021 Sep 15;10(9).
770 Available from: http://dx.doi.org/10.1242/bio.058734

771 24. Mao Y, Hong K-H, Liao W, Li L, Kim S-J, Xiong Y, et al. Generation of a novel transgenic zebrafish for
772 studying adipocyte development and metabolic control. Int J Mol Sci. 2021 Apr 13;22(8):3994.

773 25. Mazzaferro E, Mujica E, Zhang H, Emmanouilidou A, Jenseit A, Evcimen B, et al. Functionally characterizing
774 obesity-susceptibility genes using CRISPR/Cas9, in vivo imaging and deep learning. Sci Rep. 2025 Feb
775 13;15(1):5408.

776 26. van der Klaauw AA, Croizier S, Mendes de Oliveira E, Stadler LKJ, Park S, Kong Y, et al. Human Semaphorin
777 3 variants link melanocortin circuit development and energy balance. Cell. 2019 Feb 7;176(4):729-
778 742.e18.

779 27. Honecker J, Ruschke S, Seeliger C, Laber S, Strobel S, Pröll P, et al. Transcriptome and fatty-acid signatures
780 of adipocyte hypertrophy and its non-invasive MR-based characterization in human adipose tissue.
781 EBioMedicine. 2022 May;79:104020.

782 28. Emont MP, Jacobs C, Essene AL, Pant D, Tenen D, Colleluori G, et al. A single-cell atlas of human and
783 mouse white adipose tissue. Nature. 2022 Mar;603(7903):926–33.

784 29. Civelek M, Wu Y, Pan C, Raulerson CK, Ko A, He A, et al. Genetic Regulation of Adipose Gene Expression
785 and Cardio-Metabolic Traits. Am J Hum Genet. 2017 Mar 2;100(3):428–43.

786 30. Kroll F, Powell GT, Ghosh M, Gestri G, Antinucci P, Hearn TJ, et al. A simple and effective F0 knockout
787 method for rapid screening of behaviour and other complex phenotypes. Elife [Internet]. 2021 Jan 8;10.
788 Available from: http://dx.doi.org/10.7554/eLife.59683

789 31. Varshney GK, Pei W, LaFave MC, Idol J, Xu L, Gallardo V, et al. High-throughput gene targeting and
790 phenotyping in zebrafish using CRISPR/Cas9. Genome Res. 2015 Jul;25(7):1030–42.

32. Wu RS, Lam II, Clay H, Duong DN, Deo RC, Coughlin SR. A Rapid Method for Directed Gene Knockout for Screening in G0 Zebrafish. Dev Cell. 2018 Jul 2;46(1):112-125.e4.

33. Stringer C, Wang T, Michaelos M, Pachitariu M. Cellpose: a generalist algorithm for cellular segmentation. Nat Methods. 2021 Jan;18(1):100–6.

34. Tandon P, Lyall Z, Cowie M, Minchin JEN. Human genetic studies and zebrafish models identify Plxna4 as a regulator of adiposity, somatic growth, and feeding behaviours [Internet]. bioRxiv. 2025 [cited 2025 Apr 18]. p. 2025.03.15.643290. Available from: https://www.biorxiv.org/content/10.1101/2025.03.15.643290v1.abstract

35. Arner E, Westermark PO, Spalding KL, Britton T, Rydén M, Frisén J, et al. Adipocyte turnover: relevance to human adipose tissue morphology. Diabetes. 2010 Jan;59(1):105–9.

36. Gustafson B, Nerstedt A, Smith U. Reduced subcutaneous adipogenesis in human hypertrophic obesity is linked to senescent precursor cells. Nat Commun. 2019 Jun 21;10(1):2757.

37. Hedbacker K, Lu Y-H, Dallner O, Li Z, Fayzikhodjaeva G, Birsoy K, et al. Limitation of adipose tissue by the number of embryonic progenitor cells. Elife [Internet]. 2020 May 26;9. Available from: http://dx.doi.org/10.7554/eLife.53074

38. Yang Loureiro Z, Joyce S, DeSouza T, Solivan-Rivera J, Desai A, Skritakis P, et al. Wnt signaling preserves progenitor cell multipotency during adipose tissue development. Nat Metab. 2023 Jun;5(6):1014–28.

39. McMenamin SK, Minchin JEN, Gordon TN, Rawls JF, Parichy DM. Dwarfism and increased adiposity in the gh1 mutant zebrafish vizzini. Endocrinology. 2013 Apr 1;154(4):1476–87.

40. Zhao J, Li H, Zhou R, Ma G, Dekker JD, Tucker HO, et al. Foxp1 regulates the proliferation of hair follicle stem cells in response to oxidative stress during hair cycling. PLoS One. 2015 Jul 14;10(7):e0131674.

41. Naudin C, Hattabi A, Michelet F, Miri-Nezhad A, Benyoucef A, Pflumio F, et al. PUMILIO/FOXP1 signaling drives expansion of hematopoietic stem/progenitor and leukemia cells. Blood. 2017 May 4;129(18):2493–506.

42. Li H, Liu P, Xu S, Li Y, Dekker JD, Li B, et al. FOXP1 controls mesenchymal stem cell commitment and senescence during skeletal aging. J Clin Invest. 2017 Apr 3;127(4):1241–53.

43. Pearson CA, Moore DM, Tucker HO, Dekker JD, Hu H, Miquelajáuregui A, et al. Foxp1 regulates neural stem cell self-renewal and bias toward deep layer cortical fates. Cell Rep. 2020 Feb 11;30(6):1964-1981.e3.

44. Fu NY, Pal B, Chen Y, Jackling FC, Milevskiy M, Vaillant F, et al. Foxp1 Is Indispensable for Ductal Morphogenesis and Controls the Exit of Mammary Stem Cells from Quiescence. Dev Cell. 2018 Dec 3;47(5):629-644.e8.

45. Liu P, Huang S, Ling S, Xu S, Wang F, Zhang W, et al. Foxp1 controls brown/beige adipocyte differentiation and thermogenesis through regulating β3-AR desensitization. Nat Commun. 2019 Nov 7;10(1):5070.

46. Dai S, Qu L, Li J, Chen Y. Toward a mechanistic understanding of DNA binding by forkhead transcription factors and its perturbation by pathogenic mutations. Nucleic Acids Res. 2021 Oct 11;49(18):10235–49.

47. Stroud JC, Wu Y, Bates DL, Han A, Nowick K, Paabo S, et al. Structure of the forkhead domain of FOXP2 bound to DNA. Structure. 2006 Jan;14(1):159–66.

829 48. Glastonbury CA, Pulit SL, Honecker J, Censin JC, Laber S, Yaghootkar H, et al. Machine Learning based
830 histology phenotyping to investigate the epidemiologic and genetic basis of adipocyte morphology and
831 cardiometabolic traits. PLoS Comput Biol. 2020 Aug;16(8):e1008044.

832 49. Kulyté A, Aman A, Strawbridge RJ, Arner P, Dahlman IA. Genome-wide association study identifies genetic
833 loci associated with fat cell number and overlap with genetic risk loci for type 2 diabetes. Diabetes. 2022
834 Jun 1;71(6):1350–62.

835 50. Ye RZ, Richard G, Gévry N, Tchernof A, Carpentier AC. Fat cell size: Measurement methods,
836 pathophysiological origins, and relationships with metabolic dysregulations. Endocr Rev. 2022 Jan
837 12;43(1):35–60.

838 51. Jeffery E, Wing A, Holtrup B, Sebo Z, Kaplan JL, Saavedra-Peña R, et al. The adipose tissue
839 microenvironment regulates depot-specific adipogenesis in obesity. Cell Metab. 2016 Jul 12;24(1):142–
840 50.

841 52. Minchin JEN, Dahlman I, Harvey CJ, Mejhert N, Singh MK, Epstein JA, et al. Plexin D1 determines body fat
842 distribution by regulating the type V collagen microenvironment in visceral adipose tissue. Proc Natl Acad
843 Sci U S A. 2015 Apr 7;112(14):4363–8.

844 53. Chau Y-Y, Bandiera R, Serrels A, Martínez-Estrada OM, Qing W, Lee M, et al. Visceral and subcutaneous
845 fat have different origins and evidence supports a mesothelial source. Nat Cell Biol. 2014 Apr;16(4):367–
846 75.

847 54. Choi E-H, Park S-J. TXNIP: A key protein in the cellular stress response pathway and a potential therapeutic
848 target. Exp Mol Med. 2023 Jul 3;55(7):1348–56.

849 55. Russell-Guzmán J, Américo-Da Silva L, Cadagan C, Maturana M, Palomero J, Estrada M, et al. Activation
850 of the ROS/TXNIP/NLRP3 pathway disrupts insulin-dependent glucose uptake in skeletal muscle of
851 insulin-resistant obese mice. Free Radic Biol Med. 2024 Sep 1;222:187–98.

852 56. Hamilton JP, Potter JJ, Koganti L, Meltzer SJ, Mezey E. Effects of vitamin D3 stimulation of thioredoxin-
853 interacting protein in hepatocellular carcinoma: TXNIP, vitamin D3 and HCC. Hepatol Res. 2014
854 Dec;44(13):1357–66.

855 57. Freeburg SH, Shwartz A, Kemény LV, Smith CJ, Weeks O, Miller BM, et al. Hepatocyte vitamin D receptor
856 functions as a nutrient sensor that regulates energy storage and tissue growth in zebrafish. Cell Rep. 2024
857 Jul 23;43(7):114393.

858 58. Chun T-H, Hotary KB, Sabeh F, Saltiel AR, Allen ED, Weiss SJ. A pericellular collagenase directs the 3-
859 dimensional development of white adipose tissue. Cell. 2006 May 5;125(3):577–91.

860 59. Li X, Zhao Y, Chen C, Yang L, Lee H-H, Wang Z, et al. Critical role of matrix metalloproteinase 14 in adipose
861 tissue remodeling during obesity. Mol Cell Biol. 2020 Mar 30;40(8):1–24.

862 60. Kirstein AS, Kehr S, Nebe M, Hanschkow M, Barth LAG, Lorenz J, et al. PTEN regulates adipose progenitor
863 cell growth, differentiation, and replicative aging. J Biol Chem. 2021 Aug;297(2):100968.

864 61. Huang W, Queen NJ, McMurphy TB, Ali S, Cao L. Adipose PTEN regulates adult adipose tissue homeostasis
865 and redistribution via a PTEN-leptin-sympathetic loop. Mol Metab. 2019 Dec;30:48–60.

866 62. Cereijo R, Quesada-López T, Gavaldà-Navarro A, Tarascó J, Pellitero S, Reyes M, et al. The chemokine
867 CXCL14 is negatively associated with obesity and concomitant type-2 diabetes in humans. Int J Obes .
868 2021 Mar;45(3):706–10.

869 63. Zachara M, Rainer PY, Hashimi H, Russeil JM, Alpern D, Ferrero R, et al. Mammalian adipogenesis
870 regulator (Areg) cells use retinoic acid signalling to be non- and anti-adipogenic in age-dependent
871 manner. EMBO J. 2022 Sep 15;41(18):e108206.

872 64. Ampudia-Mesias E, El-Hadad S, Cameron CS, Wöhrer A, Ströbel T, Saydam N, et al. SRPX emerges as a
873 potential tumor marker in the extracellular vesicles of glioblastoma. Cancers (Basel). 2022 Apr
874 14;14(8):1984.

875 65. Zou Y, Gong N, Cui Y, Wang X, Cui A, Chen Q, et al. Forkhead box P1 (FOXP1) transcription factor regulates
876 hepatic glucose homeostasis. J Biol Chem. 2015 Dec 18;290(51):30607–15.

877 66. Ma H, Sukonina V, Zhang W, Meng F, Subhash S, Palmgren H, et al. The transcription factor Foxp1
878 regulates aerobic glycolysis in adipocytes and myocytes. J Biol Chem. 2023 May 5;104795.

879

880

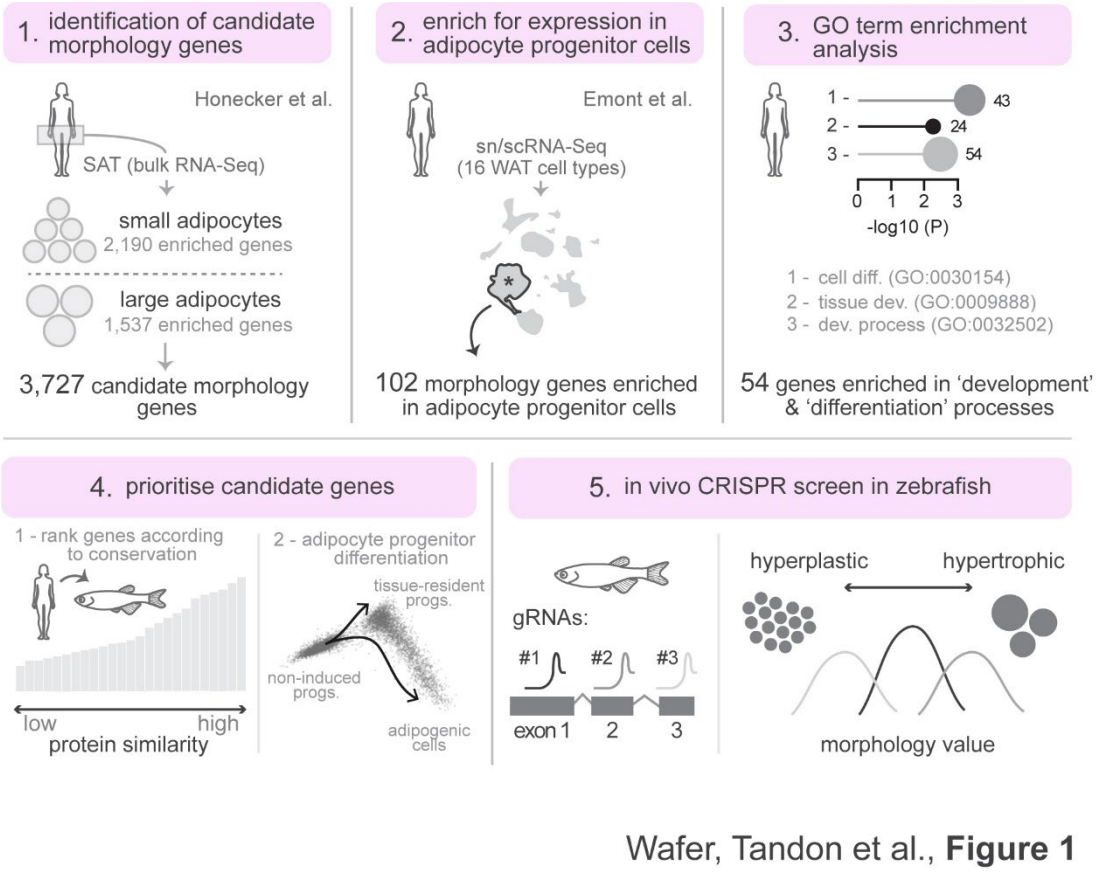

881

882 **Figure 1. Experimental workflow.** (1) Identification of candidate morphology genes from bulk RNA-
883 Seq of human subcutaneous adipose tissue (SAT), comparing genes enriched in small versus large
884 adipocytes (Honecker et al.). (2) Filtering for expression in adipose stem and progenitor cells using
885 sn/scRNA-Seq of 16 white adipose tissue (WAT) cell types (Emont et al.). (3) GO term enrichment
886 analysis to focus on genes involved in development and differentiation processes. (4) Prioritisation
887 of candidate genes based on protein conservation to zebrafish and expression dynamics during
888 adipocyte progenitor differentiation. (5) In vivo F0 CRISPR screen in zebrafish using multiple gRNAs
889 per gene to quantify lipid droplet morphology (hyperplastic versus hypertrophic).

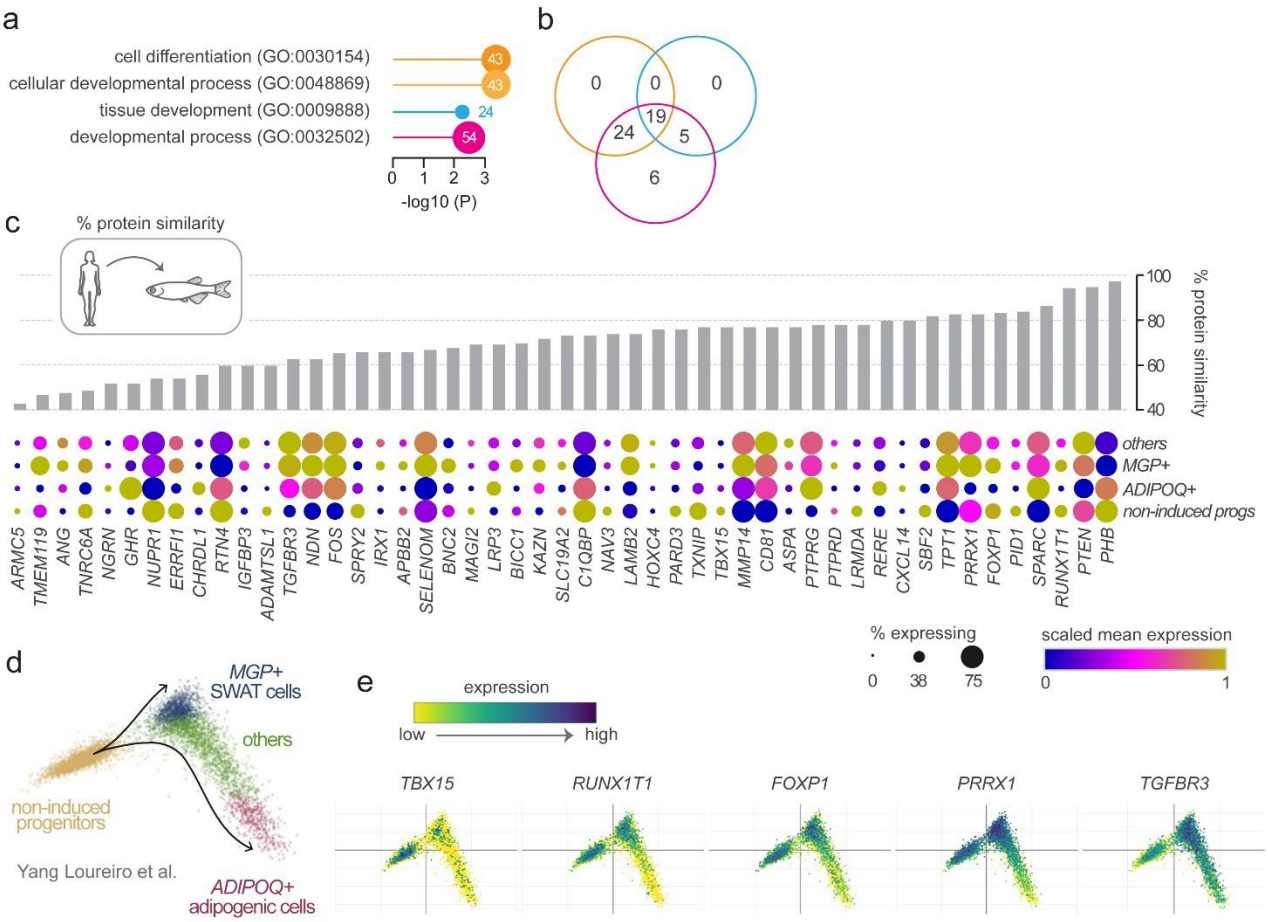

Wafer, Tandon et al., **Figure 2**

Figure 2. Prioritisation of candidate adipose morphology genes based on conservation to zebrafish and expression dynamics during progenitor differentiation. A. GO term enrichment analysis of the 102 candidate morphology genes enriched in adipose stem and progenitor cells. Four GO terms related to development and differentiation were significantly enriched, encompassing 54 genes. **B.** Venn diagram showing gene overlap between the enriched GO terms. Cell differentiation (GO:0030154) and cellular developmental process (GO:0048869) had 100% overlap. **C.** Protein conservation and expression during adipocyte progenitor differentiation for each candidate gene. Grey bars denote percentage protein similarity between human and zebrafish orthologues. Dot plots show scaled mean expression (colour) and percentage of cells expressing each gene (dot size) across four cell populations identified during in vitro progenitor differentiation: non-induced progenitors, *MGP+* SWAT cells, *ADIPOQ+* adipogenic cells and others (Yang Loureiro et al., 2023). Genes are ordered by protein similarity. **D.** PCA projection of single cells coloured by cluster designation from Yang Loureiro et al., 2023. **E.** Expression of selected candidate morphology genes projected onto the PCA embedding, illustrating enrichment during specific stages of adipocyte differentiation.

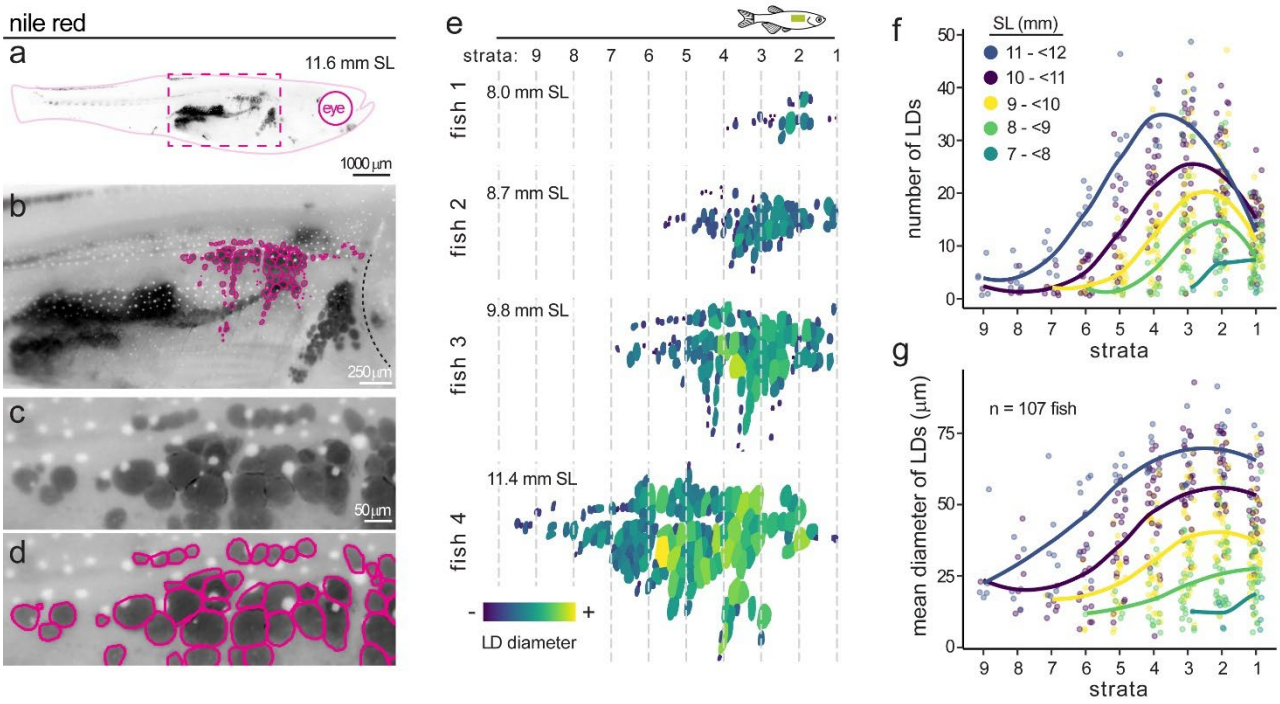

Wafer, Tandon et al., **Figure 3**

Figure 3. Spatial dynamics of subcutaneous adipose growth in zebrafish. A. Nile Red-stained zebrafish at 11.6 mm standard length (SL). Black signal denotes Nile Red-positive neutral lipid within adipose tissue. Magenta dashed box indicates the region shown in (B). **B.** Higher magnification of the subcutaneous adipose depot. Magenta outlines highlight segmented lipid droplets (LDs). Dashed line indicates the operculum. **C.** Zoomed view of individual subcutaneous adipose LDs. White dots are melanosome pigment granules. **D.** LD segmentation masks (magenta outlines) corresponding to (C). **E.** Segmented subcutaneous adipose LDs from four representative zebrafish of increasing body size, colour-coded by LD diameter. Fish sizes are shown in mm SL. Dashed lines demarcate strata defined at 200 µm intervals from the most anterior LD. **F.** Number of LDs per stratum as a function of zebrafish body size. Fish were grouped into five SL categories (colour-coded). Lines represent fitted curves; dots represent individual fish. **G.** Mean LD diameter per stratum as a function of zebrafish body size (n = 107 fish). Lines and colour coding as in (F).

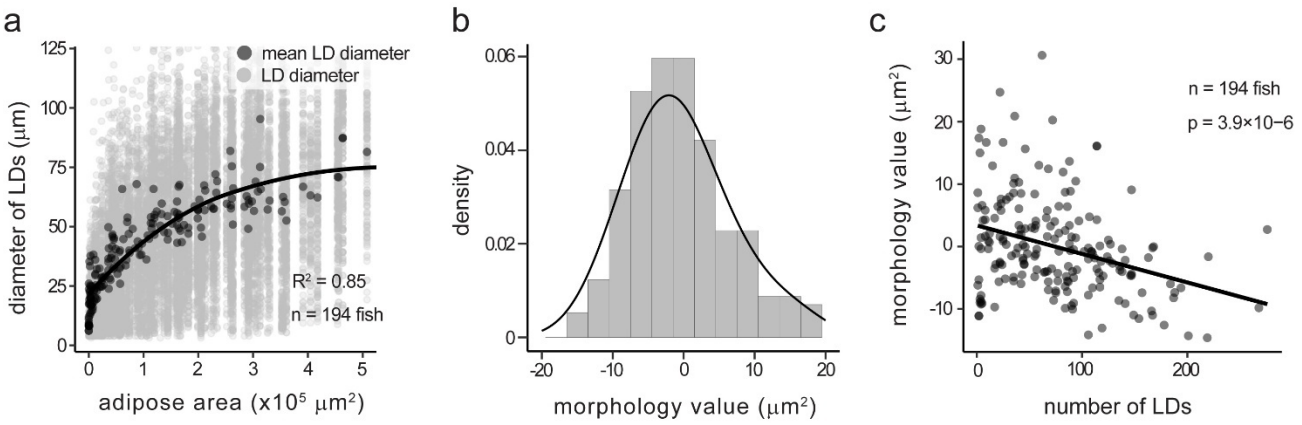

Wafer, Tandon et al., **Figure 4**

Figure 4. Derivation of the adipose morphology value from the relationship between lipid droplet size and adipose depot size. A. Diameter of subcutaneous adipose LDs plotted against total depot area. Light grey dots represent individual LDs; dark grey dots represent the mean LD diameter per fish. Black line was fitted using a generalised additive model (GAM; $R^2 = 0.85$, n = 194 fish). **B.** Distribution of morphology values, calculated as the residual deviation of each fish's mean LD diameter from the GAM fit in (A). Positive values indicate larger LDs than expected (hypertrophic); negative values indicate smaller LDs than expected (hyperplastic). Black line shows a normal density fit. **C.** Morphology value plotted against number of LDs per fish, showing an inverse relationship (linear model, $p = 3.9 \times 10^{-6}$, n = 194 fish). Fish with hypertrophic morphology tend to have fewer, larger LDs, while fish with hyperplastic morphology have more numerous, smaller LDs.

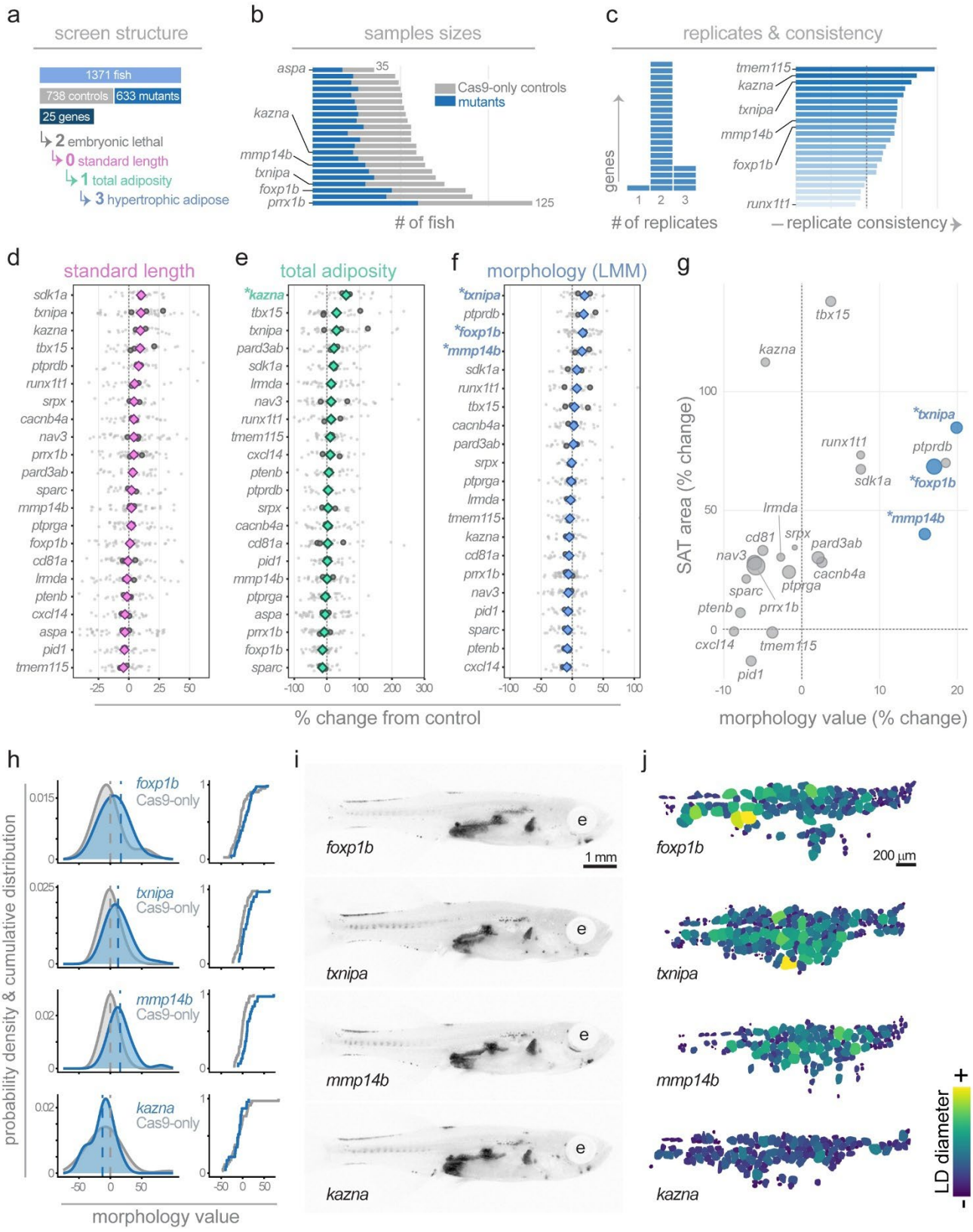

Wafer, Tandon et al., **Figure 5**

Figure 5. A targeted CRISPR screen in zebrafish identifies genes regulating hypertrophic or hyperplastic adipose morphology. A. Overview of CRISPR screen structure. In total, 1,371 fish were screened (738 Cas9-only controls and 633 mutants) across 25 candidate genes. Two genes (*phb* and

933 *rerea*) were lethal before 5 dpf. Of the remaining genes, zero altered standard length, one (*kazna*)
934 significantly increased total adiposity, and three (*txnipa*, *mmp14b* and *foxp1b*) produced significant
935 hypertrophic subcutaneous adipose morphology. **B.** Sample sizes per gene. Grey bars indicate Cas9-
936 only controls; blue bars indicate mutants. *aspa* had the smallest and *prrx1b* the largest sample size.
937 **C.** Left panel: number of experimental replicates per gene. The majority of targets had two replicates;
938 *aspa* had one replicate, and *nav3*, *prrx1b*, *tbx15* and *txnipa* had three. Right panel: replicate
939 consistency scores, representing agreement in effect direction and magnitude across replicates.
940 Genes are ordered by consistency score. **D-F.** Forest plots showing effect sizes (% change from Cas9-
941 only controls) for standard length (d, magenta), total adiposity (e, green) and morphology value (f,
942 blue). Small grey dots represent individual mutant fish; medium grey circles represent experiment
943 means; coloured diamonds represent gene-level estimates from linear mixed models (LMM) with
944 experiment as a random effect. Morphology value represents the deviation in lipid droplet Feret
945 diameter from that expected given total depot area, with positive values indicating hypertrophy and
946 negative values indicating hyperplasia. Asterisks denote BH-adjusted $p < 0.05$. **G.** Scatter plot of depot
947 (SAT) lipid area (% change from controls) versus morphology value (LMM estimate, % change from
948 controls) for each gene. Point size reflects sample size. Quadrants indicate the combination of depot
949 size and cell morphology phenotype (e.g., bigger depot with hypertrophic cells). **H.** Probability density
950 functions (left) and cumulative distribution functions (right) of morphology values for *foxp1b*, *txnipa*,
951 *mmp14b* and *kazna* F0 mutants (blue) compared with matched Cas9-only controls (grey). Dashed
952 lines indicate group means. **I.** Representative Nile Red images of *foxp1b*, *txnipa*, *mmp14b* and *kazna*
953 F0 mutants showing total adiposity. e, eye. Scale bar: 1 mm. **J.** Segmented subcutaneous adipose lipid
954 droplets from representative mutant fish, colour-coded by lipid droplet (LD) diameter. Scale bar: 200
955 µm.

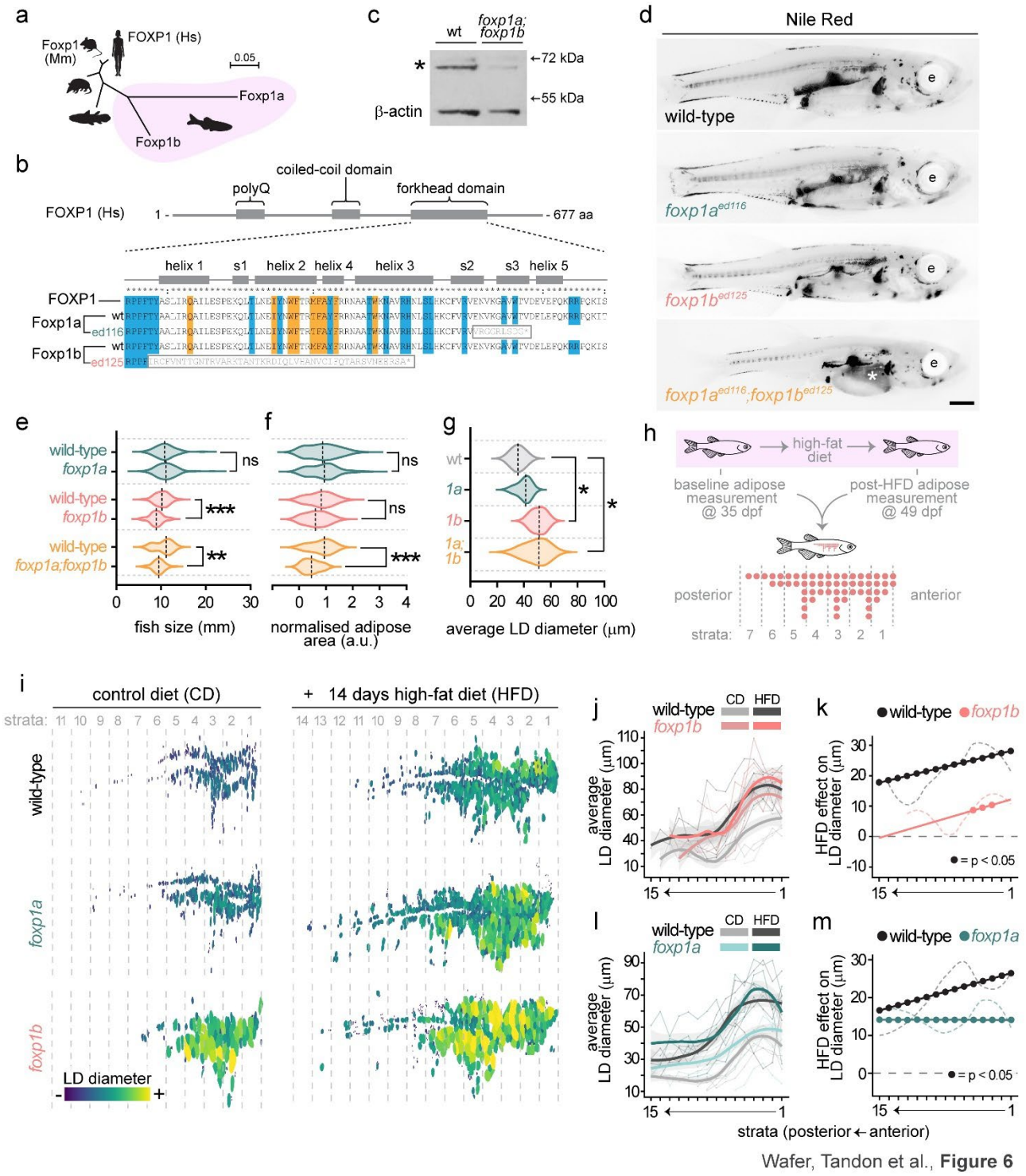

Figure 6. Stable *foxp1b* zebrafish mutants have hypertrophic adipose but undergo severely reduced hypertrophic remodelling in response to a high-fat diet. A. Phylogenetic tree showing relatedness of zebrafish Foxp1a and Foxp1b amino acid sequences to human, mouse, opossum and coelacanth Foxp1. Scale bar indicates substitutions per site. **B.** Overview of human FOXP1 domain structure showing polyglutamine (polyQ), coiled-coil and forkhead domains. Zoomed view of the DNA-binding forkhead domain showing structural features including helices (helix 1–5) and beta-strands (s1–s3). Amino acids involved in DNA binding are highlighted in blue; residues at the FOXP domain-swapped dimer interface are highlighted in orange. Wild-type zebrafish Foxp1a and Foxp1b sequences are

aligned to human FOXP1, along with the ed116 (foxp1a) and ed125 (foxp1b) mutant alleles. Grey boxes indicate the addition of nonsense peptide sequence followed by a premature stop codon. **C.** Western blot showing reduction of Foxp1 protein in foxp1a;foxp1b double mutants compared to wild-type. β-actin serves as a loading control. Asterisk indicates the Foxp1 band. **D.** Nile Red fluorescence images showing adipose lipid distribution (black signal) in wild-type, *foxp1a*^{ed116}, *foxp1b*^{ed125} and double *foxp1a*^{ed116};*foxp1b*^{ed125} zebrafish mutants. e, eye. Asterisk indicates lipid accumulation within the liver in double mutants. Scale bar is 1 mm. **E.** Violin plots of fish size (standard length, mm) in *foxp1a*^{ed116}, *foxp1b*^{ed125} and double *foxp1a*^{ed116};*foxp1b*^{ed125} mutants compared to wild-type siblings. **F.** Violin plots of normalised adipose area in the same genotypes. **G.** Violin plots of average lipid droplet (LD) diameter in the same genotypes. **H.** Schematic of the high-fat diet (HFD) feeding experiment. Zebrafish were Nile Red-imaged at 35 dpf to establish baseline adipose measurements, then subjected to a 14-day HFD (2-hour daily immersion in 5% chicken egg yolk) or control diet (2-hour daily immersion in system water), in addition to normal feeding. Post-diet Nile Red imaging was performed at 49 dpf. Subcutaneous adipose tissue was divided into anterior–posterior strata for spatial analysis. 200 μm strata are numbered anterior (1) to posterior. **I.** Segmented subcutaneous adipose LDs from representative wild-type, *foxp1a* and *foxp1b* fish on control diet (left) and after HFD (right), colour-coded by LD diameter. Strata boundaries (200 μm) are indicated by dashed lines. **J.** Average LD diameter per stratum for wild-type and *foxp1b* fish on control diet (grey or salmon) and HFD (black or pink). Thin lines represent individual fish; thick lines represent group means. **K.** HFD effect on LD diameter per stratum (HFD minus control diet) for wild-type (black) and *foxp1b* (pink). Filled circles indicate strata where the HFD effect is significant (BH adjusted $p < 0.05$). **L.** As in (J), comparing wild-type and *foxp1a*. **M.** As in (K), comparing wild-type (black) and *foxp1a* (teal). Statistical tests in (E–G) were one-way ANOVA followed by Tukey's HSD post-hoc test. $^{**}p < 0.01$, $^{***}p < 0.001$, ns = not significant.

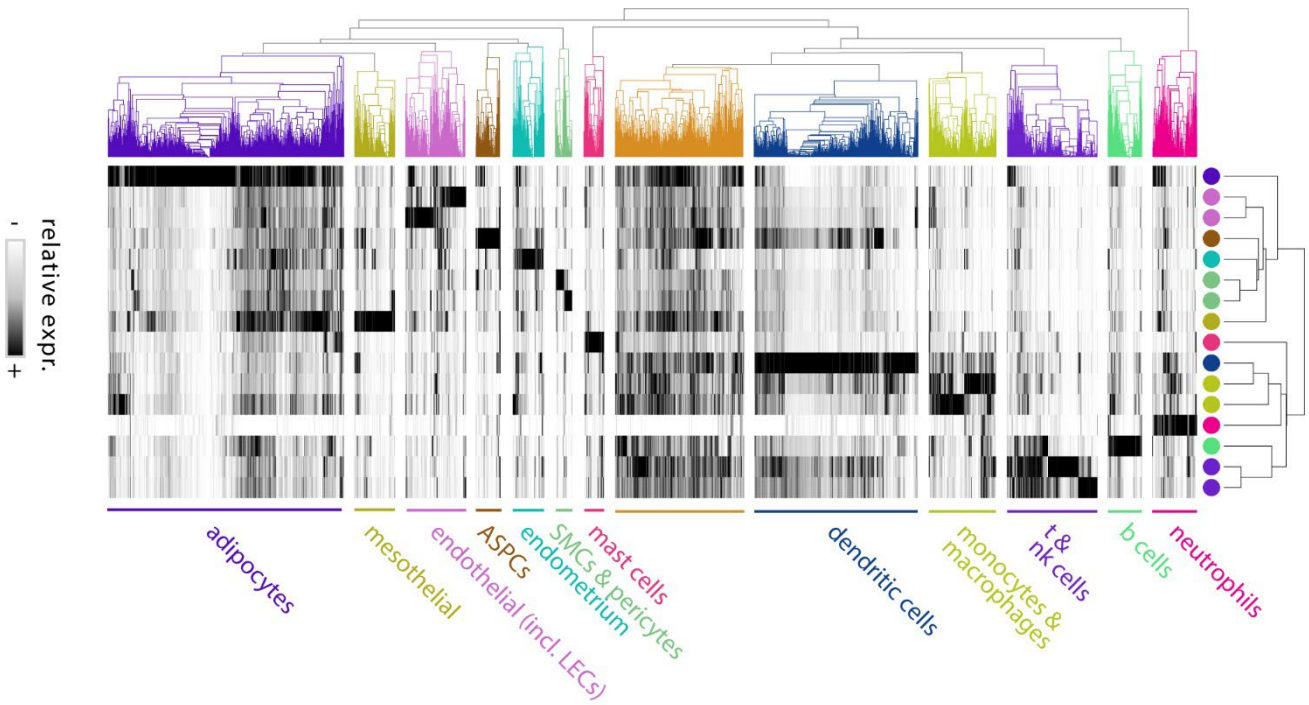

Wafer, Tandon et al., **Supplemental Figure 1**

Supplemental Figure 1. Expression clustering of candidate adipose morphology genes across human white adipose tissue cell types. Heatmap showing relative expression (log-normalised counts) of 2,980 candidate morphology-associated genes across 16 human WAT cell types from Emont et al., 2022. Genes without annotations or detectable expression in the single-cell dataset were excluded. Hierarchical clustering of genes (rows) and cell types (columns) was performed using average linkage with Pearson correlation distance. Cell types are colour-coded and labelled below: adipocytes, mesothelial cells, endothelial cells (including lymphatic endothelial cells, LECs), adipose stem and progenitor cells (ASPCs), smooth muscle cells (SMCs) and pericytes, endometrium, mast cells, dendritic cells, monocytes and macrophages, T and natural killer (NK) cells, B cells, and neutrophils. Coloured dots (right) correspond to cell type identity in the dendrogram (top).

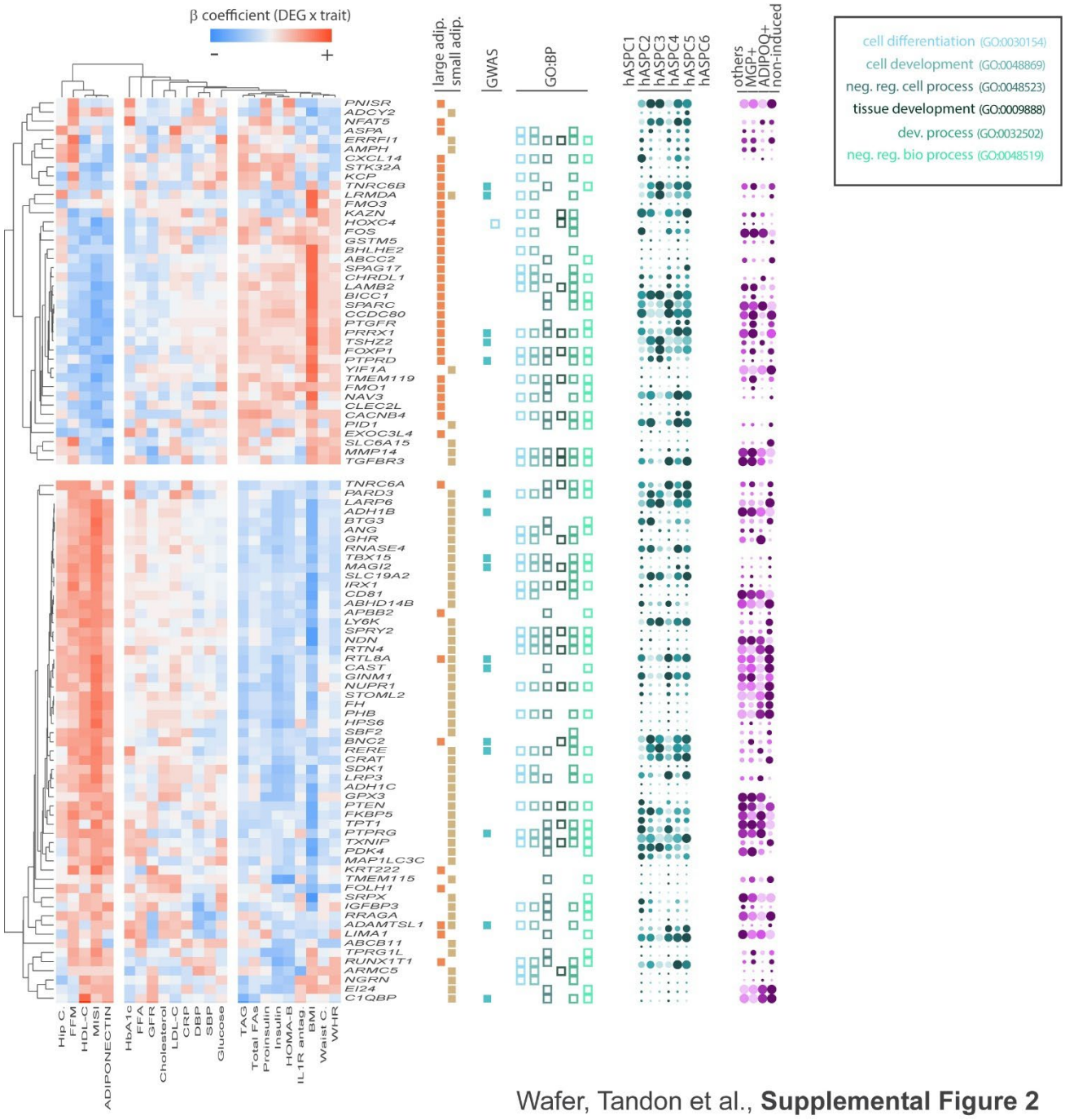

Wafer, Tandon et al., **Supplemental Figure 2**

Supplemental Figure 2. Integrative analysis of adipose morphology genes across cardiometabolic traits, GWAS loci, Gene Ontology terms, and single-cell expression profiles. The 102 candidate morphology genes enriched in adipose stem and progenitor cells (ASPCs) were characterised across multiple data sources.

Left panel: Heatmap of β coefficients from linear regression of gene expression in human subcutaneous adipose tissue (SAT) against 23 cardiometabolic traits from the METSIM cohort (Civelek et al., 2017). Blue indicates negative and red indicates positive associations. Genes and traits are hierarchically clustered. Traits include measures of body composition and adiposity (BMI, Waist C, WHR, Hip C, FFM), lipids (HDL-C, LDL-C, cholesterol, TAG, total FAs, FFA), glycaemia and insulin

1010 sensitivity (HbA1c, glucose, insulin, proinsulin, HOMA-B, MISI), inflammation (CRP, IL-1R antag.),
1011 blood pressure (SBP, DBP), renal function (GFR) and adipokines (adiponectin).

1012 Centre columns (left to right): Adipocyte size association — brown and orange bars indicate genes
1013 enriched in large or small adipocytes, respectively (Honecker et al., 2022). GWAS overlap - teal boxes
1014 indicate genes at genome-wide significant loci for BMI or WHR-adjusted BMI. GO biological process
1015 - colour-coded boxes indicate membership in enriched GO terms as shown in the legend: cell
1016 differentiation (GO:0030154), cell development (GO:0048869), negative regulation of cellular
1017 process (GO:0048523), tissue development (GO:0009888), developmental process (GO:0032502)
1018 and negative regulation of biological process (GO:0048519).

1019 Right panel: Dot plots showing expression of each gene across human WAT single-cell clusters (Emont
1020 et al., 2022 & Yang Loureiro et al., 2023). Dot size represents percentage of cells expressing; colour
1021 intensity represents scaled mean expression. Cell populations shown are: human ASPC subclusters
1022 (hASPCs1-6), MGP+, ADIPOQ+ non-induced progenitors and others.

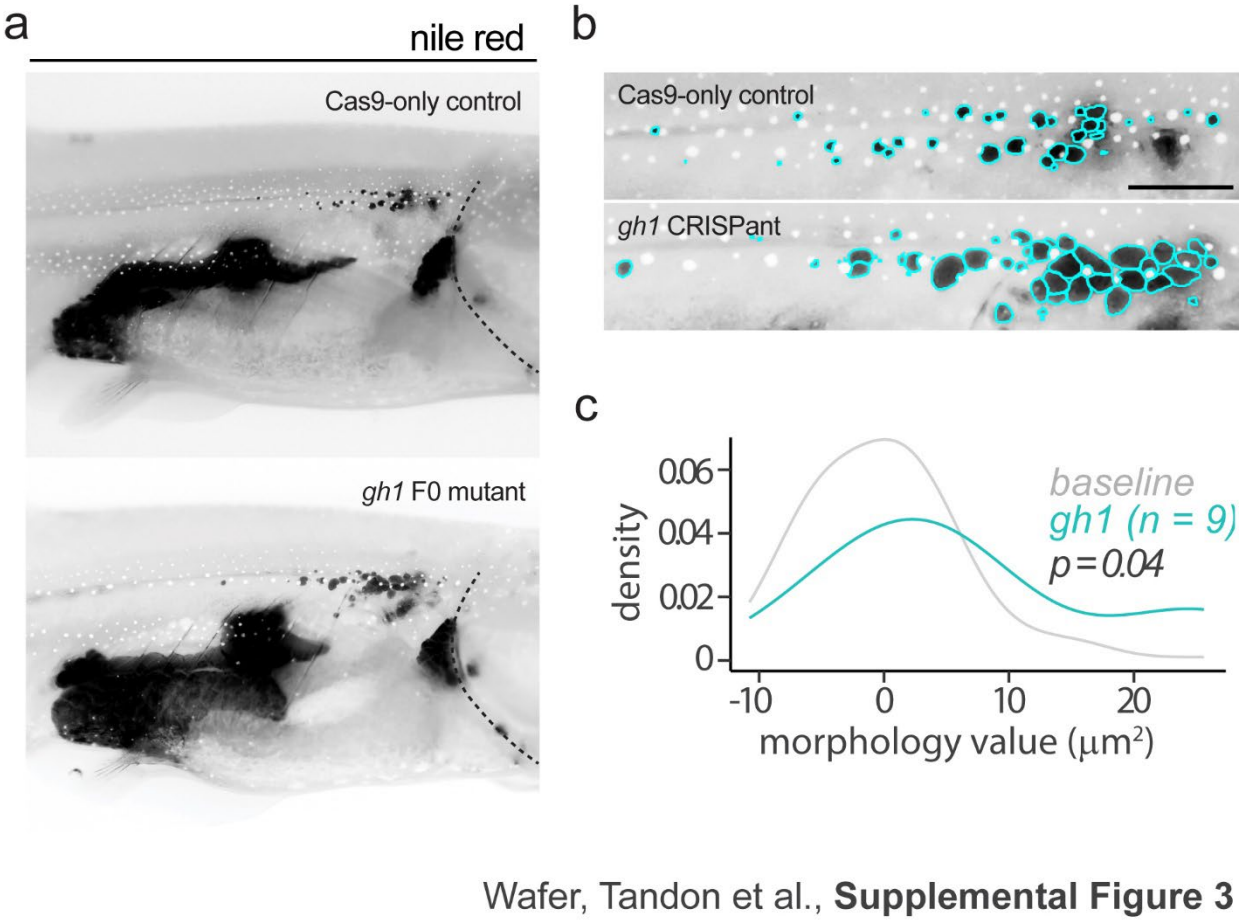

Wafer, Tandon et al., **Supplemental Figure 3**

Supplemental Figure 3. Image-based adipose morphology profiling detects hypertrophic lipid droplet expansion in *gh1* CRISPR mutants. **A.** Nile Red fluorescence images showing adiposity in a representative Cas9-only control (top) and *gh1* F0 CRISPR mutant (bottom) at ~1 month of age. Black signal denotes Nile Red-positive neutral lipid. Dotted line indicates operculum. **B.** High-magnification images of subcutaneous adipose tissue (SAT) from Cas9-only control and *gh1* CRISPant zebrafish. Cyan outlines show automated segmentation of individual lipid droplets (LDs). **C.** Kernel density plot of morphology values for *gh1* mutants (n = 9, cyan) compared to baseline wild-type fish (n = 194, grey). Morphology values were significantly increased in *gh1* mutants (Kolmogorov–Smirnov test, p = 0.04), indicating a shift toward hypertrophic morphology.

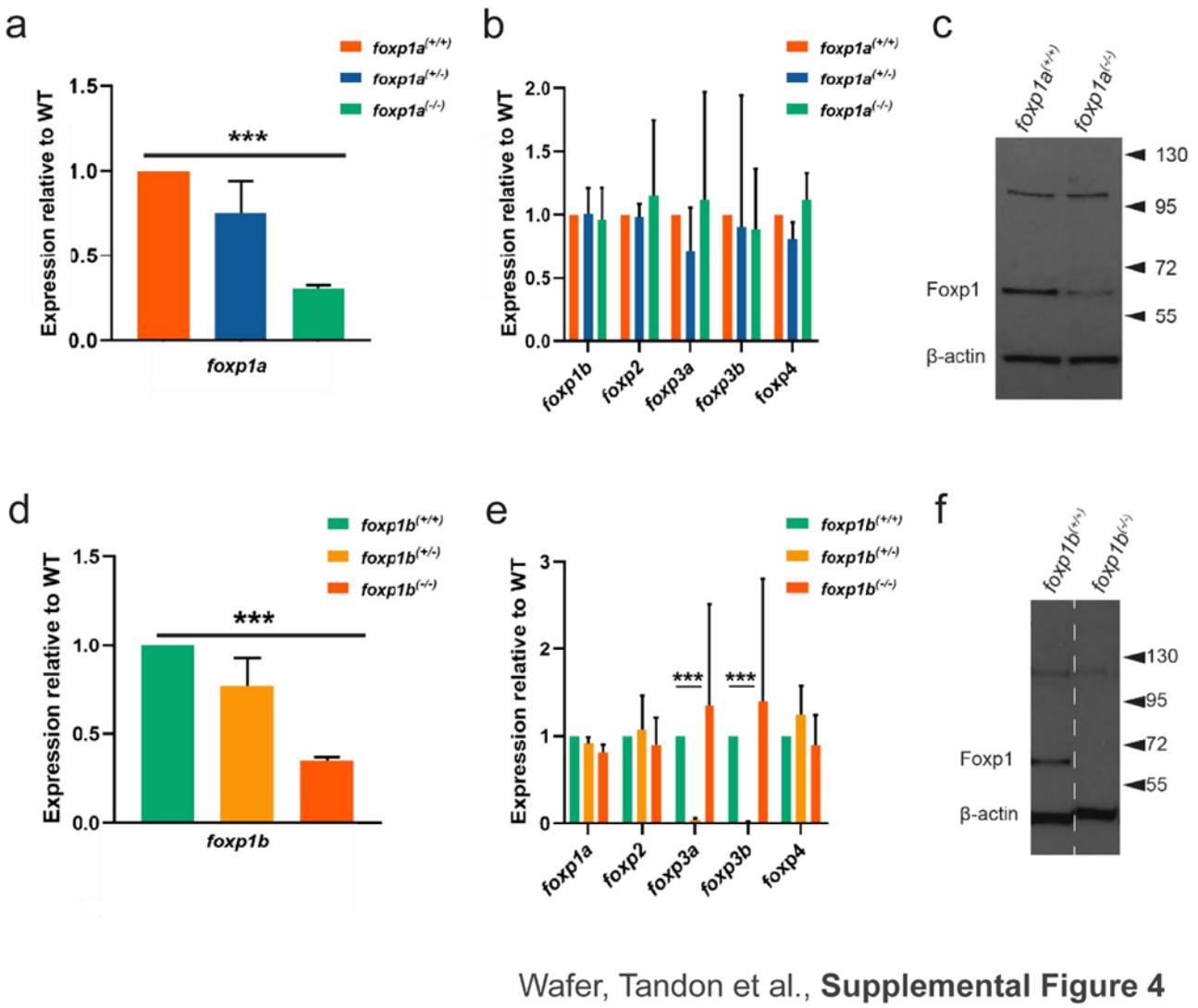

Wafer, Tandon et al., **Supplemental Figure 4**

Supplemental Figure 4. Stable *foxp1a* and *foxp1b* mutant alleles lead to reduced transcript and protein expression. A. qRT-PCR showing significantly reduced *foxp1a* mRNA expression in homozygous *foxp1a*^{ed116} mutants compared to heterozygotes and wild-type siblings. **B.** Expression of other foxp1 family genes in *foxp1a*^{ed116} mutants shows no evidence of compensatory upregulation. **C.** Western blot of Foxp1 protein in *foxp1a* wild-type (+/+) and *foxp1a*^{ed116} mutant caudal fin lysates. Foxp1 protein is markedly reduced in mutants. β-actin serves as a loading control. **D.** qRT-PCR showing significantly reduced *foxp1b* mRNA in *foxp1b*^{ed125} mutants compared to heterozygotes and wild-type siblings. **E.** Expression of other foxp family genes (*foxp1a*, *foxp2*, *foxp3a*, *foxp3b*, *foxp4*) in *foxp1b*^{ed125} mutants. *foxp3a* and *foxp3b* are significantly downregulated in heterozygotes, however this likely reflects defective amplification in those samples as homozygous mutants show no change. **F.** Western blot of Foxp1 protein in *foxp1b* wild-type (+/+) and *foxp1b*^{ed125} caudal fin lysates, showing reduced Foxp1 protein in mutants. β-actin was used as a loading control. Error bars represent standard error of the mean (SEM). ***$p < 0.001$, by unpaired two-tailed t-test.

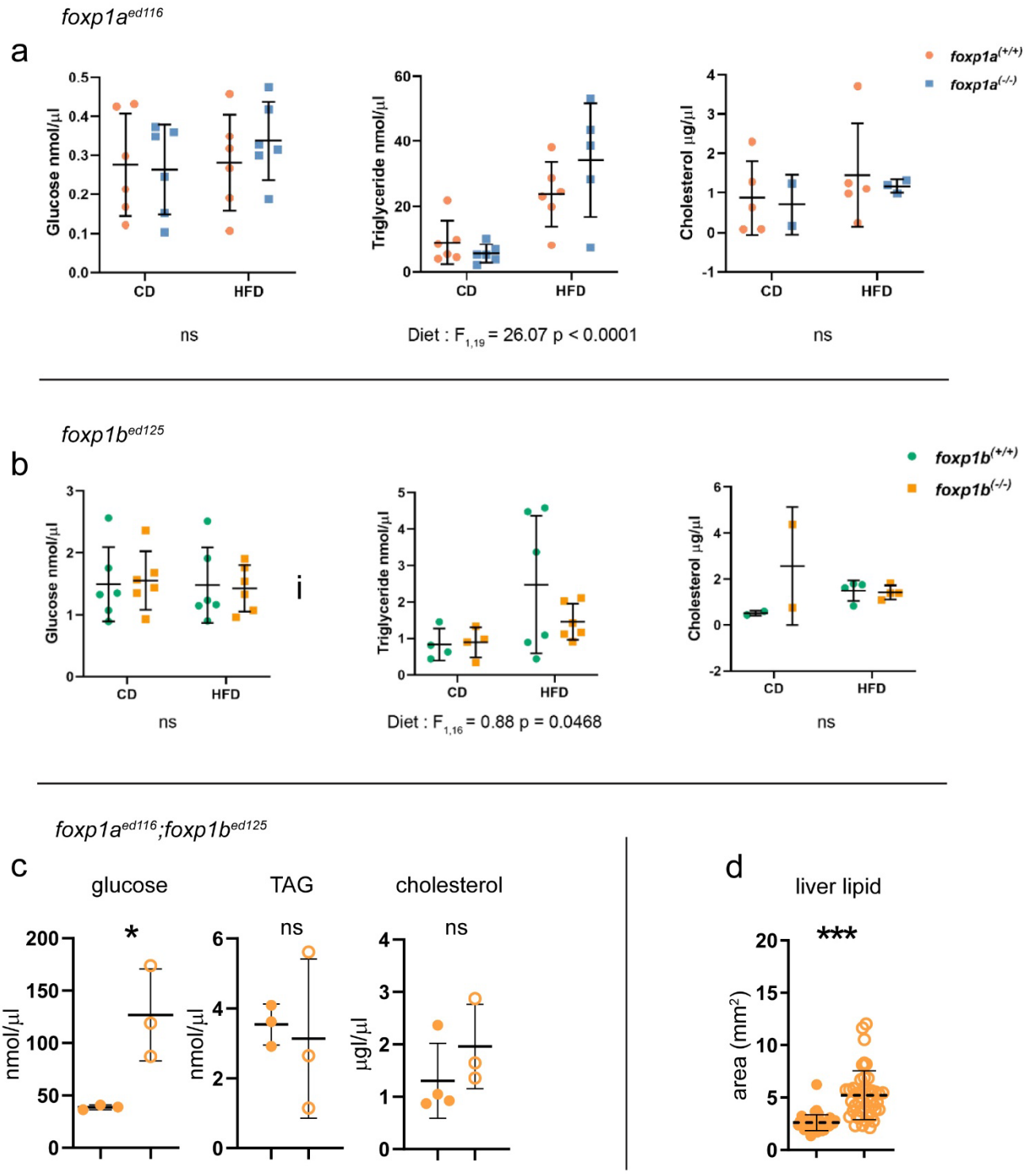

Wafer, Tandon et al., **Supplemental Figure 5**

Supplemental Figure 5. Metabolic phenotypes of *foxp1a*, *foxp1b*, and *foxp1a;foxp1b* mutant zebrafish following dietary challenge. A. Plasma glucose, triglyceride (TAG), and cholesterol levels in *foxp1a*^{ed116} mutants and wild-type siblings under control diet (CD) or high-fat diet (HFD) conditions. HFD induced a significant increase in TAG across genotypes (two-way ANOVA: F<1,19 = 26.07, p < 0.0001). No significant genotype or diet effects were observed for glucose or cholesterol. **B.** Plasma glucose, TAG, and cholesterol in *foxp1b*^{ed125} mutants and wild-type controls under CD and HFD. TAG

levels were modestly influenced by diet (two-way ANOVA: $F_{1,16} = 0.88$, $p = 0.0468$), with no significant effects detected for glucose or cholesterol. **C.** Circulating glucose, TAG, and cholesterol levels in *foxp1a*^{ed116};*foxp1b*^{ed125} double mutants. Double mutants exhibited significantly elevated glucose levels ($p < 0.05$, unpaired t-test), while TAG and cholesterol levels were unchanged. **D.** Quantification of liver lipid accumulation in *foxp1a*^{ed116};*foxp1b*^{ed125} double mutants revealed significantly increased hepatic lipid deposition compared to controls ($p < 0.001$, unpaired t-test). Error bars represent standard deviation (SD). ns = not significant.

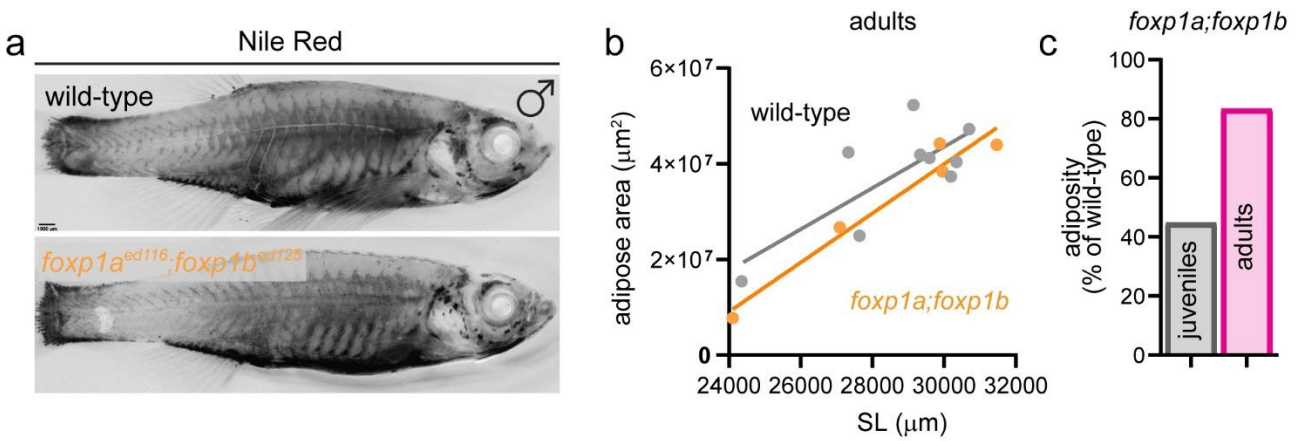

Wafer, Tandon et al., **Supplemental Figure 6**

Supplemental Figure 6. Adiposity in adult *foxp1a^{ed116};foxp1b^{ed125}* zebrafish mutants. A. Representative Nile Red-stained images of adult male wild-type and *foxp1a^{ed116};foxp1b^{ed125}* double mutant zebrafish. Lipid-rich adipose tissue appears as dark black signal. Scale bar = 1 mm. **B.** Total adipose area plotted against standard length (SL, μm) in adult wild-type (grey) and *foxp1a;foxp1b* mutants (orange). A regression line is fitted for each group, showing reduced adiposity in mutants relative to controls (μm2). **C.** Comparison of adiposity in *foxp1a;foxp1b* mutants relative to wild-type siblings at juvenile and adult stages. While adiposity was markedly reduced in juveniles, it recovered to ~80% of wild-type levels by adulthood.

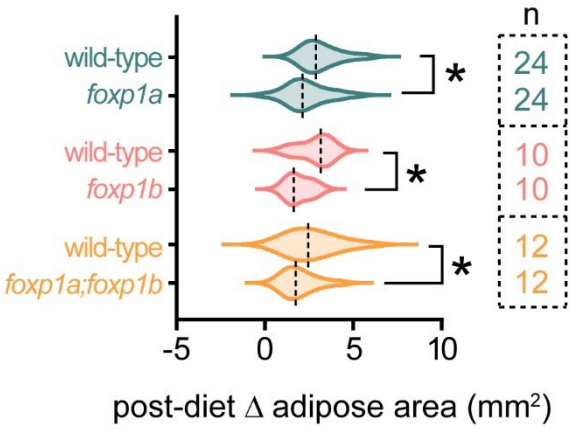

Wafer, Tandon et al., **Supplemental Figure 7**

Supplemental Figure 7. Impaired adipose expansion in all *foxp1* mutant genotypes following high-fat diet. Violin plots showing change in subcutaneous adipose area (Δ adipose area) after two weeks of high-fat diet (HFD) exposure in wild-type and *foxp1a*^{ed116}, *foxp1b*^{ed125}, and double mutant *foxp1a*^{ed116}*;foxp1b*^{ed125} zebrafish. All three mutant genotypes exhibited significantly reduced adipose expansion compared to wild-type controls, indicating impaired capacity to remodel adipose in response to nutritional excess. Sample sizes are shown at right. Asterisks indicate statistically significant differences (*$p < 0.05$), by one-way ANOVA followed by Tukey's HSD post-hoc test.

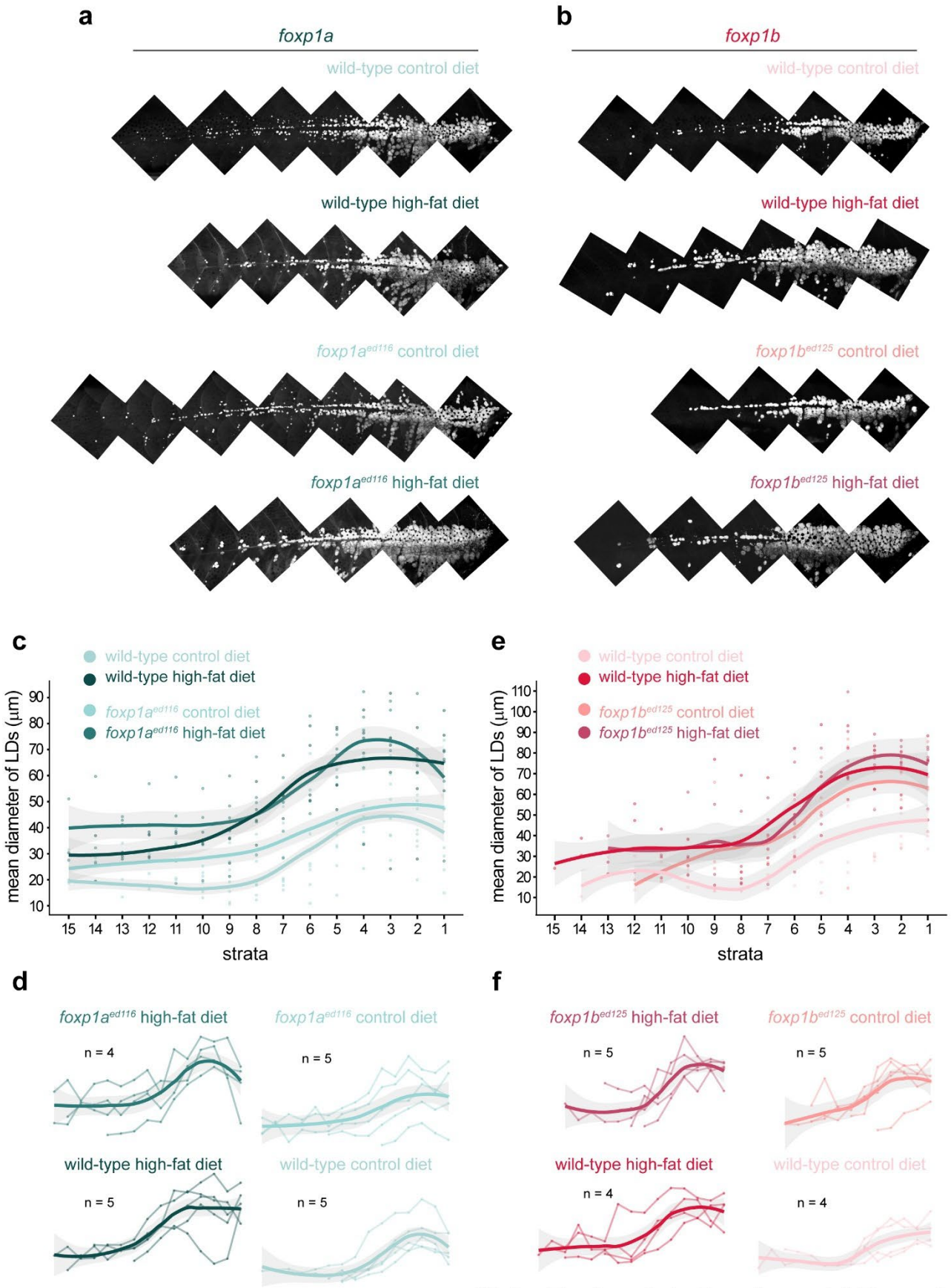

Wafer, Tandon et al., **Supplemental Figure 8**

1079 **Supplemental Figure 8. Spatial analysis of lipid droplet size along the anterior–posterior axis in**
1080 **foxp1a and foxp1b mutants following high-fat diet challenge. A.** Representative Nile Red
1081 fluorescence montages of the subcutaneous adipose depot in wild-type and *foxp1a*^{ed116} fish under
1082 control diet (CD) and high-fat diet (HFD) conditions. **B.** Representative Nile Red montages of wild-
1083 type and *foxp1b*^{ed125} fish under CD and HFD conditions. **C.** Mean lipid droplet (LD) diameter (µm) per
1084 200 µm stratum along the anterior–posterior axis for wild-type (grey) and *foxp1a*^{ed116} mutants (teal)
1085 under CD (light) and HFD (dark). Lines represent LOESS fits with shaded 95% confidence intervals;
1086 dots represent individual stratum means per fish. Strata are numbered from anterior (1) to posterior
1087 (15). **D.** Individual fish traces for each group in the *foxp1a* experiment. Thin lines represent individual
1088 fish; thick lines with shading represent group means. Sample sizes are indicated. **E.** Mean LD diameter
1089 per stratum for wild-type (grey) and *foxp1b*^{ed125} mutants (pink/red) under CD and HFD, plotted as in
1090 (C). **F.** Individual fish traces for each group in the *foxp1b* experiment, plotted as in (D).

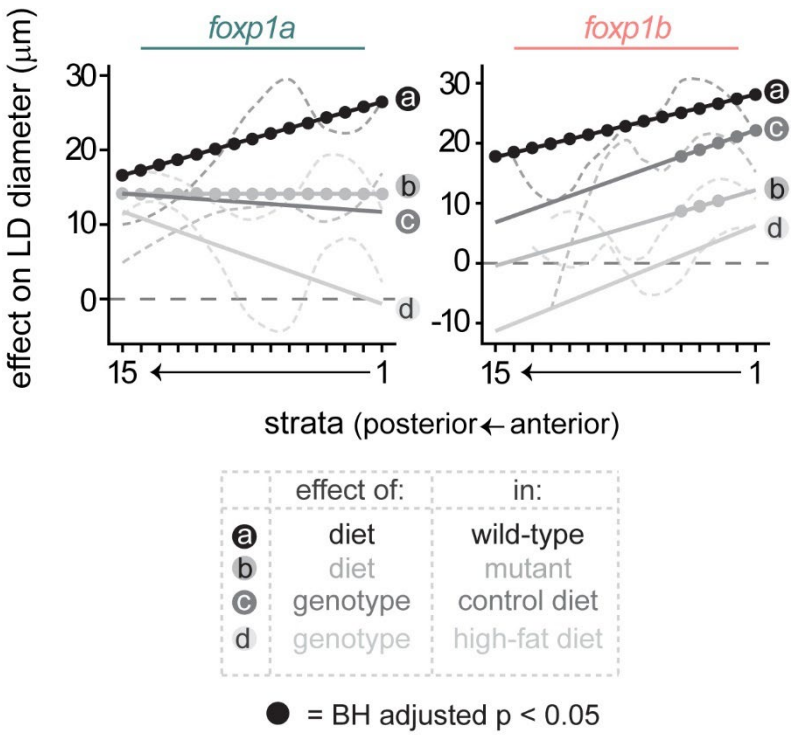

Wafer, Tandon et al., **Supplemental Figure 9**

Supplemental Figure 9. Decomposition of diet and genotype effects on lipid droplet size across the anterior–posterior axis in foxp1a and foxp1b mutants. Effect on mean LD diameter (µm) is plotted per 200 µm stratum for *foxp1a*^{ed116} (left) and *foxp1b*^{ed125} (right) experiments. Four contrasts are shown: (a) diet effect (HFD minus control) in wild-type siblings (black); (b) diet effect in mutants (dark grey); (c) genotype effect (mutant minus wild-type) under control diet (medium grey); (d) genotype effect under high-fat diet (light grey). Dashed horizontal line indicates zero effect. Filled circles denote strata where the effect was statistically significant (Benjamini–Hochberg adjusted $p < 0.05$).